Swirl–induced hysteresis in a sudden expansion flow

Article *in* Physics of Fluids · October 2024

DOI: 10.1063/5.0231799

4 authors:

Thomas Holemans
KU Leuven
14 PUBLICATIONS **56** CITATIONS
SEE PROFILE

Zhu Yang
Dongfang Electric Corporation
13 PUBLICATIONS **55** CITATIONS
SEE PROFILE

Johan De Greef
KU Leuven
34 PUBLICATIONS **525** CITATIONS
SEE PROFILE

Maarten Vanierschot
KU Leuven
143 PUBLICATIONS **1,922** CITATIONS
SEE PROFILE

Swirl-Induced Hysteresis in a Sudden Expansion Flow

T. Holemans,[1] Z. Yang,[1] J. De Greef,[2] and M. Vanierschot[1,3]

[1)]*KU Leuven, Department of Mechanical Engineering, Group T Leuven Campus, Leuven, Belgium.*

[2)]*KU Leuven, Sustainable Materials Processing and Recycling (SeMPeR), Group T Leuven Campus, Leuven, Belgium.*

[3)]*North-West University, Material Science, Innovation and Modelling (MaSIM), Mmabatho, South Africa.*

(*Corresponding author: maarten.vanierschot@kuleuven.be)

(Dated: 8 October 2024)

Swirling sudden expansion flows are complex flow fields containing several coherent structures that depend on the swirl number and can exhibit hysteresis behavior between increasing and subsequently decreasing swirl levels. While these flows have extensively been studied in simple geometries, results involving special designed nozzles are scarce. Therefore, this paper aims to provide insights into a more complex geometry, specifically a two-step conical expansion with a converging outlet. Experimental data is acquired for changing swirl numbers at a Reynolds number in the range of $35,000$. Stereoscopic Particle Image Velocimetry (S-PIV) is employed to characterize downstream flow structures, while Laser Doppler Velocimetry (LDV) is used to characterize upstream structures and to determine the inlet swirl number. Several distinct flow patterns are found as a function of the swirl number and the identified flow patterns include, in order of increasing swirl, a Closed Jet Flow (CJF), an Open Jet Flow (OJF), and a Coandã Jet Flow (CoJF). A central positive axial velocity is noted for both OJF and CoJF downstream of the expansion due to the converging outlet geometry. At higher swirl numbers, Vortex Breakdown (VB) moves upstream into the nozzle until a negative axial velocity is noted in the inlet tube. For these higher swirl numbers, no hysteresis is observed in the inlet tube between increasing and subsequently decreasing swirl. However, downstream of the nozzle, it is observed that the CoJF detaches at a lower swirl number than the swirl number required for attachment, indicating a hysteresis effect between in- and decreasing swirl.

Keywords: Swirl-induced hysteresis; Stereoscopic Particle Image Velocimetry; Laser Doppler Velocimetry; Swirling flow; Sudden expansion flow

I. INTRODUCTION

Swirling flows are crucial in various engineering applications, such as aeronautics, combustion, cyclone separators, and Ranque-Hilsch tubes, amongst others[1]. Over several decades, swirling flows have proven effective in stabilizing fast-reacting flows in burners and gas turbines, enhancing flame stability and reducing pollutants in these applications[2,3]. Additionally, it has facilitated innovations in gasoline and diesel engines and industrial furnaces, and other sectors[1]. The significant impacts of swirl are widely recognized, including increased jet growth, enhanced entrainment, and a faster decay rate compared to non-swirling jets. These effects become more pronounced at higher levels of swirl[4]. Recently, novel applications for swirling flows have emerged in the chemical sector, particularly in liquid-solid mixing. The enhanced mixing properties of swirling flows are leveraged to maintain a suspension of solid particles in a liquid in an Swirling Flow Reactor (SFR)[5].

Different flow patterns can arise in a swirling flow, depending on the swirl number, geometry, and Reynolds number (Re), amongst others. Common coherent structures in swirling sudden expansion flows include the Precessing Vortex Core (PVC)[6], self-excited jet precession[7] or Vortex Breakdown (VB)[8]. VB occurs when the swirl number surpasses a specific threshold in a sudden expansion round jet[8,9]. Despite extensive research, there is still no consensus on the underlying mechanisms of VB.[10–15].

Axial and radial confinements notably impact the flow characteristics in laminar swirling jets[16] or in nanofluid flows.[17–19]. Furthermore, contraction ratio and shape of the outlet influence upstream flow patterns[20–23]. All these studies[20–23] consider a sudden contraction and an aspect ratio (L/D) lower than 5.25. A contraction ratio ($CR = {}^{D}/_{d_{outlet}}$) above 2.56 with an aspect ratio of 4 results in a combination of VB and a positive axial central velocity[20]. In addition to geometrical parameters, the initial swirl distribution can modify the flow pattern following a sudden expansion[8,24]. To summarize, a diverse range of parameters influence the behavior of swirling jet flows and their associated flow patterns.

In the computational work of Moise and Mathew [14], a transitional Reynolds number of $1,000$ was examined. The study involved the manipulation of swirl numbers, both increasing and decreasing. A difference in radial expansion in two identical swirl number regions was observed, resulting in a hysteresis. At intermediate swirl numbers, a bi-stability of Bubble-shaped Vortex Breakdown (BVB) and Conical-shaped Vortex Breakdown (CVB) occurred, while regular CVB

and wide-open CVB types were bi-stable at higher swirl numbers.

Regular CVB and wide-open CVB have been classified as Open Jet Flow (OJF) and Coandã Jet Flow (CoJF), respectively. This classification is used mainly for swirling sudden expansion flows[25,26]. When a stepped conical expansion flow is combined with an annular inlet tube, the OJF can be classified into two sub-classes, i.e., Low-Swirl and High-Swirl. The OJF - Low Swirl has a conical VB behind the annular obstruction. For the OJF - High Swirl, the CVB radially expands to attach to the conical wall of the first sudden expansion. This sub-classification does not apply in cases without a stepped inlet[27,28], so for the remaining text only the main classification of OJF will be used. Similar to a CVB wide-open shape, CoJF is a flow field in which the flow attaches to the bottom wall perpendicular to the expansion.

Swirling sudden expansion flows exhibit hysteresis behavior in both laminar and turbulent regimes when increasing and subsequently decreasing the swirl. For $Re = 180$ and $11,000$, respectively discussed in Ogus, Baelmans, and Vanierschot[26] and Vanierschot and Van den Bulck[29], the flow transitions from a Closed Jet Flow (CJF) to an OJF-Low Swirl until finally reaching the OJF-High Swirl flow state. After decreasing the swirl, it transitions to a CoJF state, and the flow remains attached to the wall until no inlet swirl is present anymore[26,29]. Increasing the step size in an annular jet, Vanierschot and Van den Bulck[30] have shown that an unstable CoJF can be reached while increasing swirl number without any hysteresis noted.

Computational Fluid Dynamics (CFD)-simulations have demonstrated the working principles of an SFR, achieving a CoJF at moderately high swirl numbers[5], in both one-phase and two-phase flows. A CoJF is essential in an SFR as it mitigates solid sedimentation due to its flow attachment to the bottom wall of the reactor. The current study provides an experimental basis of one-phase flow structures present in an SFR and their relation to inlet swirl number. Achieving a CoJF at low swirl numbers decreases the pressure drop across the swirl generator, increasing the efficiency of the system. Experimental validation is necessary to explore the possibility of achieving a CoJF at low swirl numbers due to hysteresis effects.

Hysteresis between an CJF, OJF and CoJF has only be observed in annular jet flows, where the interaction between a central and corner recirculation zone plays a major role in the flow pattern choice. In this study, the nozzle geometry is adapted to a two-step conical nozzle to achieve hysteretic behavior in a round jet as well. To the author's knowledge, multi-step conical round jet expansions are not considered in the literature, especially not their hysteresis behavior, which is only studied numerically for transitional round jets[14] or numerically and experimentally for

annular jets[26,29]. This paper presents experimental flow field measurements in a two-step conical expansion. Using Laser Doppler Velocimetry (LDV), the inlet flow is characterized, followed by Stereoscopic Particle Image Velocimetry (S-PIV) measurements of downstream flow fields at different swirl numbers, both increasing and decreasing. The flow states are identified as CJF, OJF, and CoJF. A discussion of the hysteresis behaviour is included. Contrary to one-step expansions, the OJF is found to be more stable than the CoJF in this two-step conical expansion[26,29].

II. EXPERIMENTAL SETUP AND DATA PROCESSING

A. Geometry

The geometry considered is an SFR for solid-liquid mixing processes[5,31]. It comprises a sudden expansion with a step of $0.15\,d_i$ and two tapered parts for which the dimensions are depicted in Figure 1, where d_i refers to the nozzle diameter. The first tapered part has a radial dimension $0.16\,d_i$ and is installed at 20°. While the second tapered part has a radial dimension of $1.63\,d_i$ and is installed at 75°. Both angles are measured from the centerline (x-axis). Figure 2a shows a picture of the setup from the S-PIV laser's perspective.

A guide vane swirl generator, designed by Dugué and Weber[32], can feed a variable swirling flow into this sudden expansion vessel. Figure 3b depicts the guide vanes' position for maximal swirl. This swirl generator is used in numerous studies on annular swirling jets[25,27,33], and round jets[9,34,35]. The annular tube is removed in this study, and a detailed view is given in Figure 3a. Upstream of the movable block swirl generator, the flow is divided into six separate parts (yellow tubes in Figure 2a). This uniformly feeds the settling chamber, shown in Figure 3a. The swirl number is experimentally calibrated using LDV, which is explained in detail in section II B. The flow of water is regulated by a frequency-controlled centrifugal pump (Packo NP/68-50/152). Downstream of the sudden expansion vessel, it contracts at 45° to an outlet diameter of $4/3\,d_i$, as visualized at the top of Figure 1. The cylindrical and octagonal confinements are made of transparent PolyMethyl MethAcrylate (PMMA). The volume between the confinement and the cylinder is filled with water to minimize refraction issues.

B. Laser Doppler Velocimetry (LDV)

Consistent documentation of the initial conditions for studies of free shear flows is an impor-

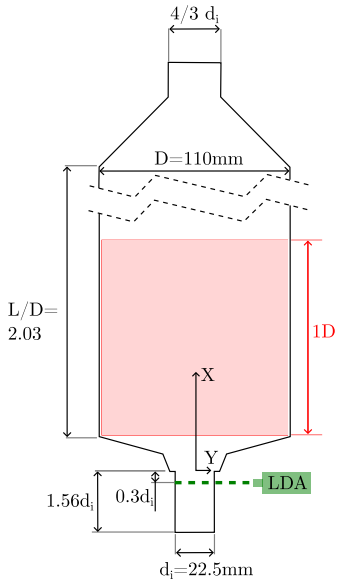

FIG. 1: Schematic drawing of the sudden expansion vessel in a side-view with the inlet at the bottom and the outlet at the top. A pink rectangle indicates the S-PIV measurement area. The measurement location of the LDV measurements is indicated by the dashed green line at $x/d_i = -0.3$.

tant aspect to allow comparison between studies[24,36–39]. The jet inlet profile of the current study is measured using a 1D LDV FiberFlow system of Dantec Dynamics. Both the profiles and their associated swirl numbers are discussed extensively in Section II E. Essential information about these measurements is included in the current section. An adjustment to the conventional swirl number is done to calibrate the inlet flow field. The conventional swirl number does eliminate the pressure term and turbulent fluctuation stresses, and an adjustment to its integration radius will change its final value. However, it can still serve as a useful estimator of the degree of swirl for categorizing swirl injectors, as long as the integration limit and axial position are specified, as discussed in detail by Vignat, Durox, and Candel[40]. Ideally, the inlet profile should be measured as close to the sudden expansion as possible, to limit errors due to a non-ideal definition of the swirl number[40]. However, at this position, the first step of the sudden expansion blocks the top laser beam when measuring the axial velocity. The closest measurement position possible is at $-6.8mm$ upstream

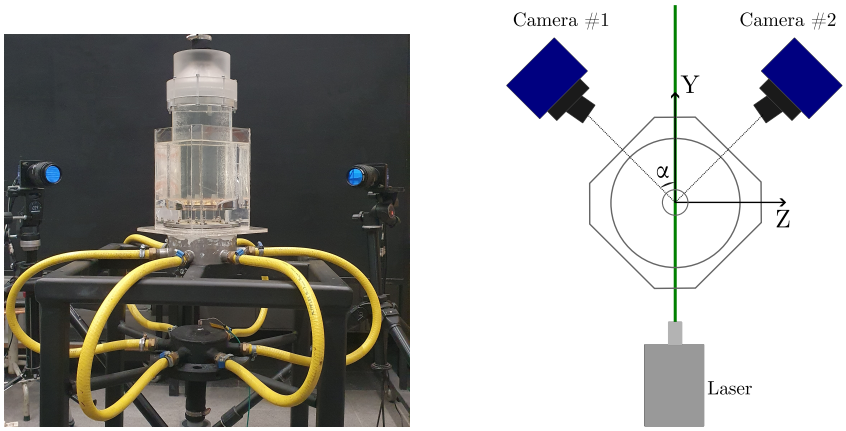

(a) (b)

FIG. 2: S-PIV configuration both in a photograph and a top-view schematic representation. (a) Photograph of the cameras and sudden expansion vessel, viewed from the laser perspective. (b) Schematic representation of the S-PIV configuration, top view.

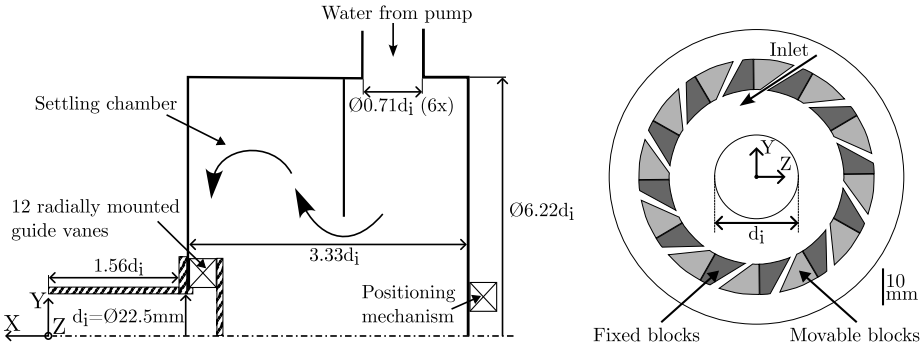

(a) (b)

FIG. 3: Schematic representation of the swirl generator and positioning of the guide vanes. (a) 30kW movable block swirl generator as designed by Dugué and Weber[32]. (b) Position of the guide vanes of the swirl generator to produce a maximal swirling inlet flow.

Optics			**Refractive indices**[41]		
Focal length	Expansion factor	Wavelength	n_{PMMA}	n_{air}	n_{water}
310 mm	1.98	532 nm	1.49	1.00	1.33

TABLE I: Details about the optics in the LDV setup and the refractive indices considered in Appendix A.

	Fringe spacing [µm]	Depth [µm]
No refractions	2.27	671
Axial measurements	2.27	896
Tangential measurements	[2.27–2.37]	[896–935]

TABLE II: Details about the fringe spacing and the depth of the measurement volume for three conditions. "No refractions," where there are no interfaces between the probe and measurement volume (added for reference). "Axial measurements," where all interfaces are straight. "Tangential measurements," where interfaces are both straight and circular, as shown in Figure 4.

($x/d_i = -0.3$), where both the axial and tangential velocity can be measured subsequently. Figure 1 shows this position as a green dotted line. The following formula calculates an adjusted swirl number ($S_{0.84}$), which is the conventional swirl number adjusted to only include 84% of the total inlet pipe's diameter (d_i). This adjustment is necessary due to refraction limitations at the pipe's edges, so the integration limit becomes $|y| = 0.42\,d_i$:

$$S_{0.84} = \frac{\int_0^{0.42\,d_i} \overline{u}\;\overline{w}\,r^2\,dr}{\frac{d_i}{2}\int_0^{0.42\,d_i} \overline{u}^2\,r\,dr}, \tag{1}$$

where r is the radial position in the inlet tube. The mean axial or tangential velocities at a specific location are denoted as $\overline{u}$ and $\overline{w}$, respectively.

Details about the optics and the refractive indices considered can be found in Table I. Due to refractions into the circular test section, the fringe spacing and measurement volume change, as indicated in Table II. The width and height of the measurement volume are nearly equal for all measurements with a value close to 79 µm.

The LDV probe is installed on an YZ-translation stage to allow for the centering of the laser and precise movement throughout the inlet tube. An axisymmetric flow field is expected based on previous studies using the same swirl generator[42,43]. This axisymmetry is used to locate the

inlet tube center for axial and tangential velocity measurements. Due to refractions, the axial and tangential velocity measurement locations are slightly different. These refractions result in a linear spatial shift for the axial measurements, which is noted in Equation 2. After locating the inlet tube's center, the subsequent displacements of the LDV probe are depicted as Δ. The actual measurement location at this probe's position is $x_{6,axial}$. In essence, a fixed displacement of the measurement volume also occurs. This is, however, irrelevant since the center of the tube is determined by a calibration measurement, so only the movement of the probe needs to be scaled linearly, with its corresponding scaling factor according to Equation 2,

$$x_{6,axial} = \frac{tan(\alpha_1)\Delta}{tan\left(arcsin(\frac{n_{air}}{n_{water}}\alpha_1)\right)}. \tag{2}$$

For the tangential measurements, the interfaces at the tube are circular, resulting in a non-linear spatial shift and a shift in the physical properties of the LDV's measurement volume. This is visually represented for one measurement position in Figure 4. Both the fringe spacing and the measurement volume change throughout the measurements with the range indicated in Table II. The geometric variables, indicated on Figure 4 are p_1=5.0 mm, p_2=10.0 mm, L_1=73.8 mm, and $R = d_i/2$=11.2 mm. The first angle (α_1) and y_1 are properties of the LDV probe and its optics. All intersection points between an interface and the laser beam are identified with their respective x- and y-coordinates. The relationship between the position of the LDV probe (L_1) and the actual measurement position (x_6) is determined using Equations A1 to A14, explained in Appendix A. These equations are based on trigonometry and Snell's law. The measured velocities with the LDV hardware and software are corrected to represent the correct velocities.

C. Stereoscopic Particle Image Velocimetry (S-PIV)

The measurements downstream of the step are performed using S-PIV. Two cameras are positioned at angles of 49.4° and 51.5°, with reference to the normal vector of the laser sheet, corresponding to α in Figure 2. The laser is positioned to illuminate the center of the sudden expansion vessel as depicted in Figures 1 and 2. The two cameras used are Imager SX6M cameras equipped with an AF Micro-Nikkor 60mm f/2.8D lens. The laser is a 200 mJ pulsed laser of Litron with a wavelength of 532 nm. Fluorescent Red Microspheres (FRM) from Cospheric with a density of $\rho = 995\ kg/m^3$ and a diameter of $40-47\ \mu m$ are used as seeding particles. The combination of an

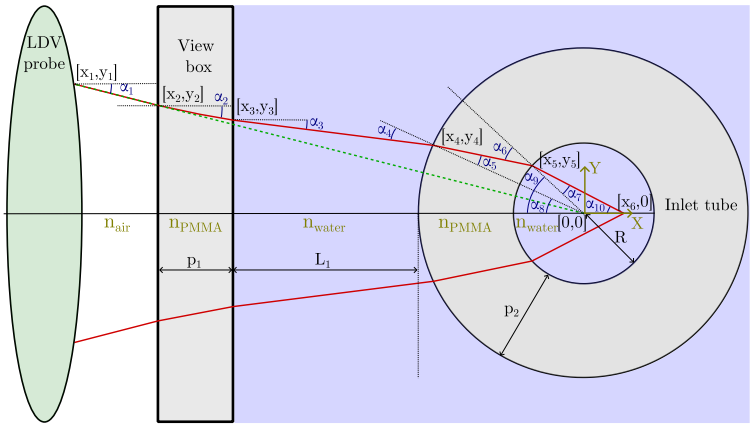

FIG. 4: Visualization of the refractions in the inlet pipe due to the different medium interfaces for tangential velocity measurements. The green dashed line shows the expected laser path without any refractions, which would measure in the exact center of the tube. The red line shows the actual line the laser will follow based on the refractions between each medium interface. The grey areas show all PMMA materials. The purple region represents the water inside the inlet tube and surrounding the inlet tube within the view box.

optical edge filter at a wavelength of 540nm on both cameras and fluorescent particles minimize laser reflections near the walls. By using a 3D calibration plate, any remaining refraction errors are corrected. Self-calibration is also performed to adjust for possible misalignment in the laser sheet during the original calibration. The acquired images are processed to obtain velocity fields by Davis 10.1.2, by a multi-pass algorithm with two final passes of interrogation windows 32×32, featuring an overlap of 50%. The final spatial resolution of the vectors is 0.77 *mm*. After each interrogation pass, two criteria are used to delete possible erroneous vectors. Firstly, any vector showing a correlation value lower than 0.5 is removed. Secondly, a 4-pass regional median filter deletes vectors if they deviate more than 3 standard deviations from the regional median. If the second or third highest peak in correlation values does not deviate more than four standard deviations from the regional median, they replace the original highest peak vector. These two post-processing steps are also applied to the final vector field. Finally, any vectors missing after these post-processing steps are interpolated from their neighbors.

D. Accuracy of optical measurement techniques

Errors from both LDV and S-PIV measurements are similar to a certain extent. The errors in both measurements can be divided into systematic and random errors[44]. The systematic errors are mainly due to misalignment in the setup and tracing accuracy of the seeding particles. The former is kept as small as possible by carefully aligning the laser sheet and the calibration plate for S-PIV. The latter is achieved since the seeding particles' Stokes number is sufficiently low[45]. Any setup's misalignment will result in a large erroneous radial velocity originating from projection errors, which interpret the tangential velocity as a radial velocity. The centering of the laser is fine-tuned based on subsequent measurements, in which the non-physical central radial velocity due to misalignment is minimized.

Both measurement techniques are spatially low-pass, averaging the flow, with S-PIV having a larger filter than LDV. For the LDV data, due to the non-uniform sampling rate, both axial and tangential velocities are corrected using a transit time weighing on the raw measurement data to correct for any statistical bias towards higher velocities, as described by Buchhave, George, and Lumley[46], and George[47].

Random errors are quantifiable based on statistics. The uncertainties on both the mean and the standard deviation can be calculated as[48]:

$$\delta_{\overline{u}} = \sigma_{\overline{u}_{true}} \sqrt{\frac{1}{N_{eff}}} Z_{\alpha/2}, \qquad \delta_{\sigma_{\overline{u}}} = \sigma_{\overline{u}_{true}} \sqrt{\frac{1}{2(N_{eff}-1)}} Z_{\alpha/2}, \tag{3}$$

where $\delta_{\overline{u}}$ is the uncertainty of the time-averaged velocity component and $\delta_{\sigma_{\overline{u}}}$ is the uncertainty of the standard deviation. $Z_{\alpha/2}$ is 1.96 for a 95% confidence interval. The effective number of samples N_{eff} is determined for each location based on Equation 4[48]:

$$N_{eff} = \frac{N}{\sum_{n=0}^{+\infty} \rho(n\Delta t)}, \tag{4}$$

where N is the total number of snapshots and $\rho(n\Delta t)$ is the auto-correlation of these samples, of which a summation is taken. The summation is stopped once the correlation values reach zero for the first time. True standard deviation ($\sigma_{\overline{u}_{true}}$) is determined by the following formula for S-PIV[48]:

$$\sigma^2_{\overline{u}_{true}} = \sigma^2_{\overline{u}} - \overline{\delta^2_u}, \tag{5}$$

where $\sigma_{\overline{u}}$ is the standard deviation, which is the sum of $\sigma_{\overline{u}_{true}}$ (true standard deviation) and $\overline{\delta^2_u}$ (mean square of instantaneous measurement uncertainty). For LDV $\sigma_{\overline{u}_{true}}$ is equal to $\sigma_{\overline{u}}$, due to it

being an absolute measurement technique. Representative profiles of $\overline{u}$ and $\sigma_{\overline{u}}$ with their corresponding uncertainties, $\delta_{\overline{u}}$ and $\delta_{\sigma_{\overline{u}}}$, are plotted at multiple sections in the sudden expansion vessel in Appendices II and III for all S-PIV measurements. The calculations for v and w are identical to the ones above. The LDV results with their corresponding error bars for each measurement are plotted in Figure 5.

E. Calibration of the swirl generator

The LDV measurements' Reynolds number is $33,000 \pm 2,000$, calculated as $Re = \frac{\overline{u}_{inlet} d_i \rho}{\mu}$. This Reynolds number corresponds to the flow in a 30kW swirl burner, for which the swirl generator was initially designed. However, this Reynolds number is also representative for higher Reynolds numbers, usually found in industrial-sized setups, as the hysteresis is Reynolds independent in the turbulent regime[25]. The swirl number is gradually increased by rotating the movable blocks inside the swirl generator with a servo motor. An Arduino controls this motor, and a correction for the gear's backlash is included. The average inlet flow velocity in the nozzle ($\overline{u}_{inlet}$) and the temperature of the liquid are measured for each data set. The tangential data set is scaled to correspond to the same inlet flow speed as the axial data set for calculating each swirl number. The flow rate is within 10.9% similar and the Reynolds number within 5.6%, for subsequent axial- and tangential measurements. An important note is that the axial and tangential velocities are measured for increasing swirl numbers. The swirl numbers for decreasing swirl have the same geometrical inlet flow as the corresponding increasing swirl case. This simplification has been validated by measuring three radial positions for both increasing and decreasing swirl numbers, and no difference is observed between these. Figure 5 shows the normalized axial and tangential velocity for each geometrical configuration of the swirl generator.

A high level of axisymmetry is observed between $y/d_i \leq 0$ and $y/d_i > 0$, depicted as blue and red, respectively. This axisymmetry is similar to previous studies using the same swirl generator[34,42,43]. $S_{0.84}$ is calculated for both $y/d_i \leq 0$ and $y/d_i > 0$, of which the average results in the final value for $S_{0.84}$.

For $S_{0.84} = 0$ and 0.10 (Figures 5a and 5b), the axial velocity profile is similar to a power law velocity profile[49], with $S_{0.84} = 0.10$ evolving more towards a top-hat profile[38,50,51]. The tangential profile fluctuates around zero for $S_{0.84} = 0$. At $S_{0.84} = 0.10$, the tangential profile increases until $|y|/d_i = 0.2$, leveling at 0.15. From $S_{0.84} = 0.27$ (Figure 5c) onwards, the gradient of the axial

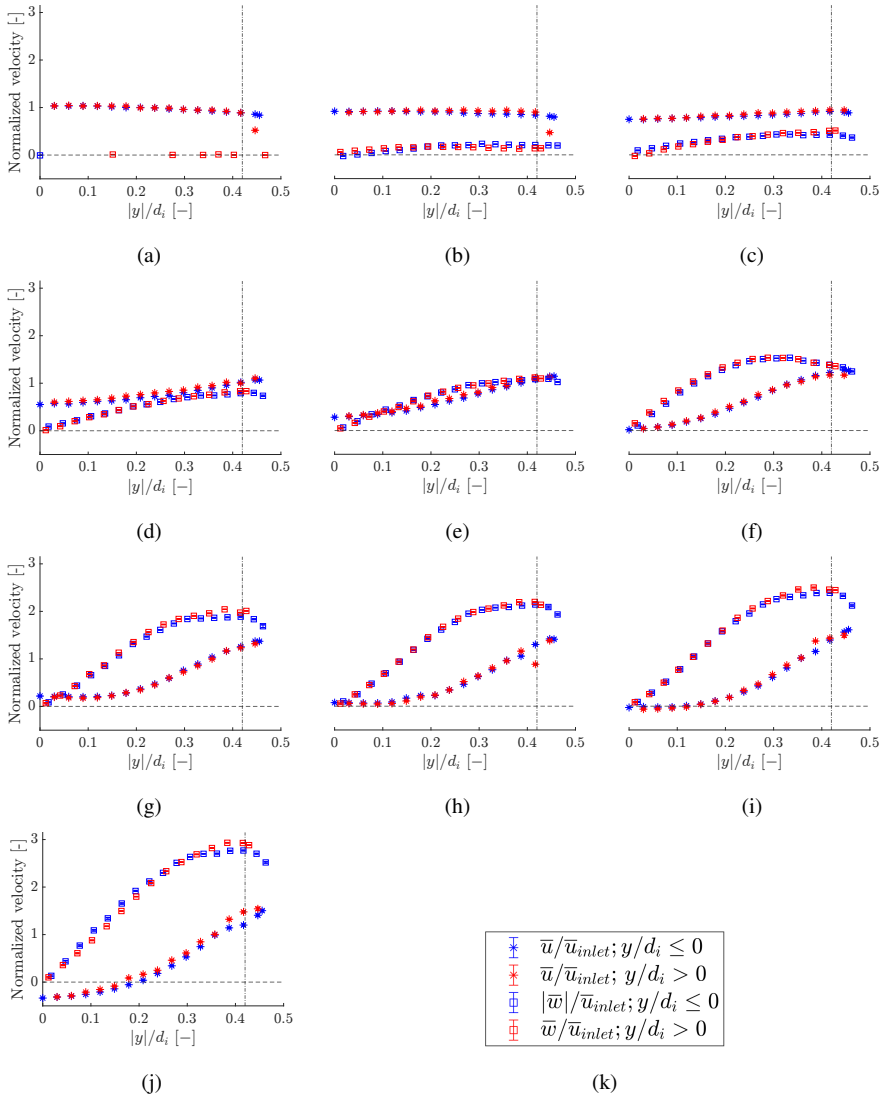

FIG. 5: Axial and tangential velocity profiles at $x/d = -0.3$, measured with LDV, for different swirl settings of the swirl generator. A dash-dotted vertical line is shown at the limit value of $|y|/d_i = 0.42$, utilized in Equation 1. A dashed horizontal line is shown to indicate a zero-velocity. (a) $S_{0.84} = 0$. (b) $S_{0.84} = 0.10$. (c) $S_{0.84} = 0.27$. (d) $S_{0.84} = 0.48$. (e) $S_{0.84} = 0.73$. (f) $S_{0.84} = 1.13$. (g) $S_{0.84} = 1.50$. (h) $S_{0.84} = 1.65$. (i) $S_{0.84} = 1.74$. (j) $S_{0.84} = 1.95$. (k) Legend for plots 5a to 5j.

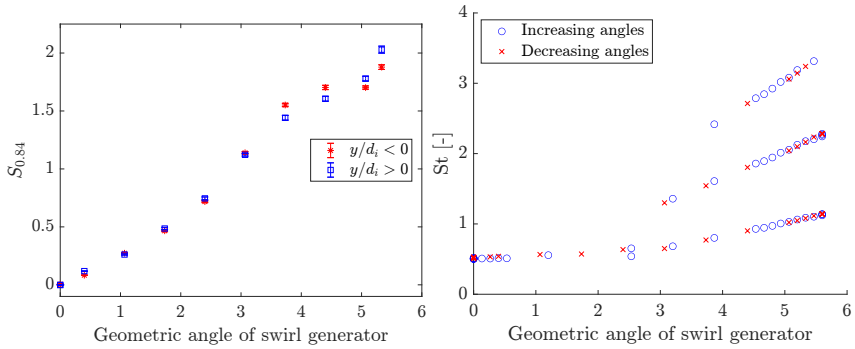

(a) (b)

FIG. 6: Both the swirl number and its corresponding frequencies for different geometrical settings of the swirl generator. (a) Geometric angle of the swirl generator with its corresponding swirl number ($S_{0.84}$), with both the positive and negative side depicted. (b) Geometric angle of the swirl generator with its corresponding frequencies obtained from a Power Spectral Density (PSD), including their hysteresis behavior. Each measurement is done at $y/d_i = 0.38$.

profile increases towards the edge of the inlet pipe.

The center velocity of the axial velocity profile decreases with increasing swirl, as can be observed in Figure 5. At $S_{0.84} = 1.74$ (Figure 5i) a central recirculation appears. This is expected since, at high swirl numbers, the recirculation zone associated with VB enters the nozzle[52,53].

The LDV data is used to identify frequencies present in the inlet flow field. A representative PSD plot, shown in Figure 7a, illustrates tangential velocity measurements of $S_{0.84} = 1.95$ at $y/d_i = 0.38$. The PSD employs Welch's method[54], providing a smoother profile with a spectral resolution of 0.004. Multiple criteria define peaks in the PSD: they must exceed $-30dB$, possess a prominence of at least $6dB$, and amount at least twice the mean value of surrounding samples when considering 15 spectral points on each side of the respective peak. Prominence defines the peak to its intrinsic height by defining it as the minimum decrease between the current peak and any higher neighboring peaks. The PSD depicted in Figure 7a shows three identifiable peaks adhering to these criteria. While stricter criteria could be applied, these might overlook low-power harmonics. The established settings effectively identify most peaks while minimizing erroneous identifications. For low swirl numbers, $S_{0.84} = 0.10 - 0.27$, only faint peaks in the tangential velocity spectra are observed, with only one or two complying with the criteria, as depicted in

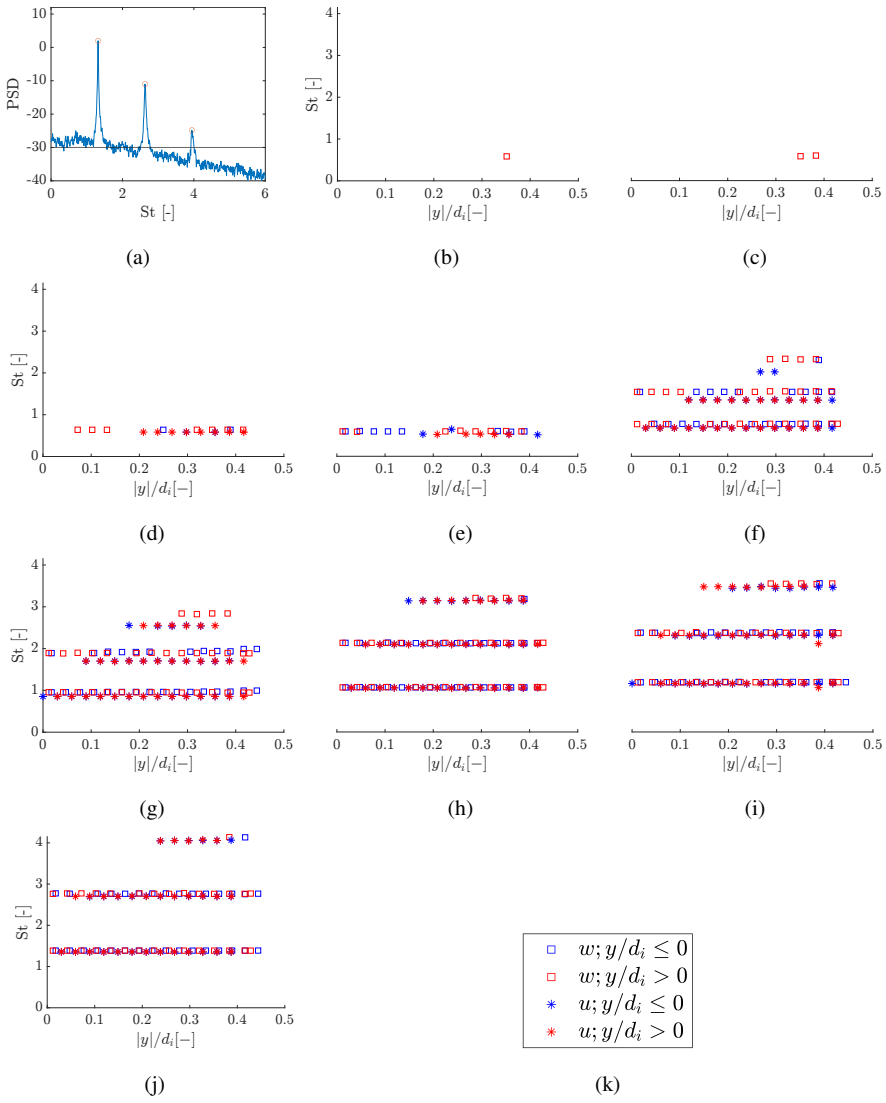

FIG. 7: Strouhal number ($St = {}^{f\,d_i}/_{\overline{u}_{inlet}}$) obtained from a PSD for the axial and tangential velocity measurements at $x/d = -0.3$, measured with LDV, for different swirl settings of the swirl generator. (a Example of a PSD spectrum for $S_{0.84} = 1.95$ and $y/d_i = 0.38$. (b) $S_{0.84} = 0.10$. (c) $S_{0.84} = 0.27$. (d) $S_{0.84} = 0.48$. (e) $S_{0.84} = 0.73$. (f) $S_{0.84} = 1.13$. (g) $S_{0.84} = 1.50$. (h) $S_{0.84} = 1.65$. (i) $S_{0.84} = 1.74$. (j) $S_{0.84} = 1.95$. (k) Legend for plots 7b to 7j.

Figures 7b and 7c. From $S_{0.84} = 0.48$ onwards, consistently similar values emerge throughout the nozzle's PSD analysis. Notably, from $S_{0.84} = 1.13$ onwards, multiple peaks are observed in the PSD spectrum, indicating harmonics. As the swirl number increases, the energy content of the coherent structure and its harmonics grows. For $S_{0.84} = 1.13$, $S_{0.84} = 1.50$ & $S_{0.84} = 1.74$, a deviation appears between the axial and tangential Strouhal number, most likely due to the frequency jitter. The structures and their harmonics are more present between $0.2 < |y|/d_i < 0.4$, as is depicted in Figure 7. At $|y|/d_i > 0.4$, the acquisition rate of the LDV probe is lower due to a lower sensitivity setting to counteract the wall reflections. This lower acquisition rate lowers the highest frequency observable in the spectrum. The acquired value for $S_{0.84}$ for different swirl generator positions, both for $y/d_i \leq 0$ and $y/d_i > 0$, is depicted Figure 6a.

Similar Strouhal numbers and harmonics have been observed in previous studies[5,6,33]. Vanierschot *et al.*[33] studied an annular swirling jet with a swirl number of 0.36, identifying both a single and double helical PVC ($St = 0.27$ & $St = 0.56$), the latter being not a harmonic of the former. For a similar inlet geometry to this study, with the adjustments of an annular outlet and two-phase flow, Yang *et al.*[5] observed a PVC ($St \approx 1$) and its second harmonic ($St \approx 2$) for a swirl number of 1.7, using CFD simulations. Syred[6] summarized studies demonstrating a linear relationship between Strouhal and swirl numbers, which found similar values as discussed in this paper. A PVC precesses around the central axis, which is the most likely reason for being less observable in the central measurements ($|y|/d_i < 0.2$). Up to the third harmonic of the PVC is observed at the higher swirl number measurements. Figure 6b presents tangential velocity measurements' frequencies at $y/d_i = 0.38$ for various swirl numbers, both increasing and decreasing. It shows no hysteresis behavior concerning identified frequencies.

III. TIME-AVERAGED FLOW FIELDS

The S-PIV measurements acquire data at seven geometric positions of the swirl generator, while the LDV data have a slightly higher resolution with ten data points. The LDV calibration data, visualized in Figure 6a, are fitted with a logistics (also frequently called Sigmoid) function, which approaches a maximum value close to the highest geometrical input angle. This fitted function is utilized to interpolate the S-PIV swirl numbers from the LDV data. The error considered is determined as the linear interpolation of the two closest geometric angles of the LDV data set and their respective errors. Every S-PIV measurement consists of 1500 individual measurements. The

average acquisition frequency is around $7.5Hz$. The different flow patterns are identified with the three velocity components and the stream function ϕ[55],

$$\phi(x,r) = \frac{2\pi \int_0^{r_{max}} \overline{u}(x,r) r dr}{Q}, \tag{6}$$

where r_{max} is the furthest radial point for which an axial velocity is available, Q is the volumetric flow rate measured during the experiment $[m^3/s]$. In the following subsections, III A, III B and III C, a representative profile of each distinguishable flow pattern (CJF, OJF, and CoJF) is shown and discussed in detail. An overview of all measurements is given in the appendices. The mean of each velocity component and the corresponding Root Mean Square (RMS) velocity are shown in Appendices II and III, respectively, while the stream functions and in-plane vectors are depicted in Appendices IV and V, respectively.

A. Closed Jet Flow (CJF)

Figure 8 visualizes a representative flow profile of a CJF at $S_{0.84} = 0$. A CJF has streamlines in the center without any Central Recirculation Zone (CRZ), similar to jet flow. A precessing structure is present in this condition, extensively discussed in Holemans *et al.*[7]. A similar precessing structure is present in this flow field based on a Spectral Proper Orthogonal Decomposition (SPOD) analysis[56], with a Strouhal number of 0.0026, which is close to values reported by Holemans *et al.*[34]. The tangential velocity profiles are zero within measurement accuracy.

B. Open Jet Flow (OJF)

Figure 9 visualizes a representative flow profile of an OJF at $S_{0.84} = 0.35$. A similar flow field is present at $S_{0.84} = 0.16$ and 0.69. An OJF has streamlines which expand radially, recirculating to the center. Due to the geometry of the outlet, limited recirculation in the center and a positive central jet are observed. In literature, a positive central axial velocity is seen for a contraction ratio of 2.56 and higher[20], similar to the contraction ratio of 3.67 in the current study. An essential difference with previous studies is the outlet shape, which is a 45° contraction instead of a sudden one. The size of a CRZ depends on a high rate of decay of swirl velocity[22], which is not achieved due to the confinement. This leads to a small CRZ, reaching into the nozzle[23,52,53]. The decrease in central axial velocity can also be observed in the LDV measurements for increasing swirl numbers.

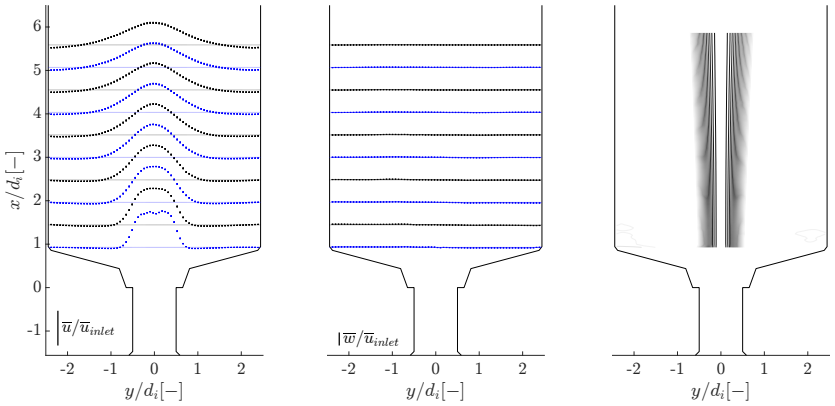

FIG. 8: Visualization of a CJF at $S_{0.84} = 0$, displayed in the geometry. Left and middle: axial and tangential velocity profiles are depicted with their error bars. Only one in two data points is shown to improve readability, and the colors alternate between black and blue to distinguish the plots easily. Right: isocontours of the stream function (ϕ(x,r)). (a) Axial velocity profiles. (b) Tangential velocity profiles. (c) Stream function (ϕ).

In the current study, the central positive velocity exists significantly further upstream, most likely due to the aspect ratio (L/D) being half of the aspect ratio considered in Li and Gutmark[20]. For the tangential velocity, a high gradient is observed in the center, which propagates through the domain. Similar behavior is seen in Escudier, Nickson, and Poole[23] with an outlet contraction ratio of 2.2.

C. Coandă Jet Flow (CoJF)

Figure 10 visualizes a representative flow profile of a CoJF at $S_{0.84} = 1.78$. A similar flow field is present at $S_{0.84} = 1.13$ and 1.52. An OJF has streamlines which strongly expand radially, attaching to the second tapered part of the inlet. This jet is simultaneously present with a central jet flow. The higher RMS values in the central region of this flow field originate from a wobbling motion of the jet, as discussed by Holemans *et al.*[34]. The recirculation zone, originating from a VB, is going further into the nozzle, which decreases the central axial velocity values, as seen in the LDV measurements. A more extensive discussion of this flow field can be found in Holemans

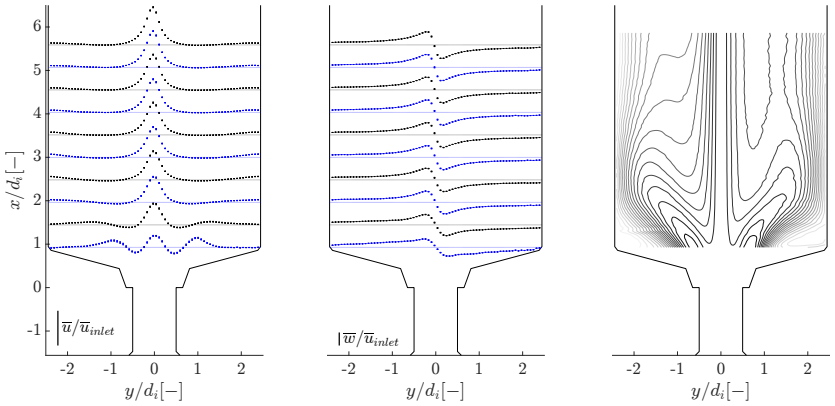

FIG. 9: Visualization of an OJF at $S_{0.84} = 0.35$, displayed in the geometry. Identical figure composition as Figure 8. (a) Axial velocity profiles. (b) Tangential velocity profiles. (c) Stream function (ϕ).

et al.[34]. From $S_{0.84} = 1.52$ onwards, a double peak axial velocity forms at a sufficient distance from the expansion. This radial expansion into two peaks also reduces the maximum velocity of these peaks.

IV. HYSTERESIS MAP

The different flow structures observed while increasing ($\uparrow$) the swirl number are identified and discussed in the previous section. When the swirl number is decreased ($\downarrow$), different flow structures are noted at the same swirl numbers, indicating hysteresis behavior. A visual representation of this hysteresis is depicted in Figure 11. A representative stream function plot of each flow state is visualized, specifically, a CJF at $S_{0.84} = 0$ (start), an OJF at $S_{0.84} = 0.69\uparrow$, and a CoJF at $S_{0.84} = 1.78\uparrow$.

The flow structures of each measurement are shown in the different appendices. A similarity in the respective flow fields is evident in several pairs of increasing and decreasing swirl numbers. Specifically, the following pairs, denoting first the increasing case and then the decreasing swirl number: $S_{0.84} = [0.16; 0.69]$ (increasing OJF), $S_{0.84} = [1.13; 1.52]$ (increasing CoJF) and $S_{0.84} = [0.35; 1.13]$ (decreasing OJF). These pairs exhibit comparable velocity profiles, RMS pro-

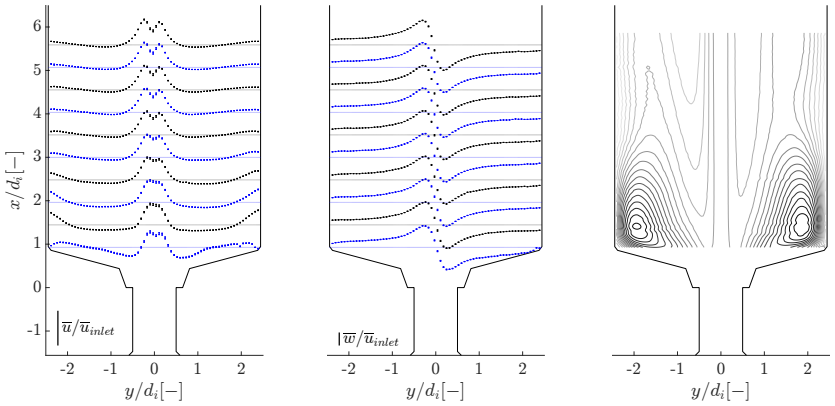

FIG. 10: Visualization of a CoJF at $S_{0.84} = 1.78$, displayed in the geometry. Identical figure composition as Figure 8. (a) Axial velocity profiles. (b) Tangential velocity profiles. (c) Stream function (ϕ).

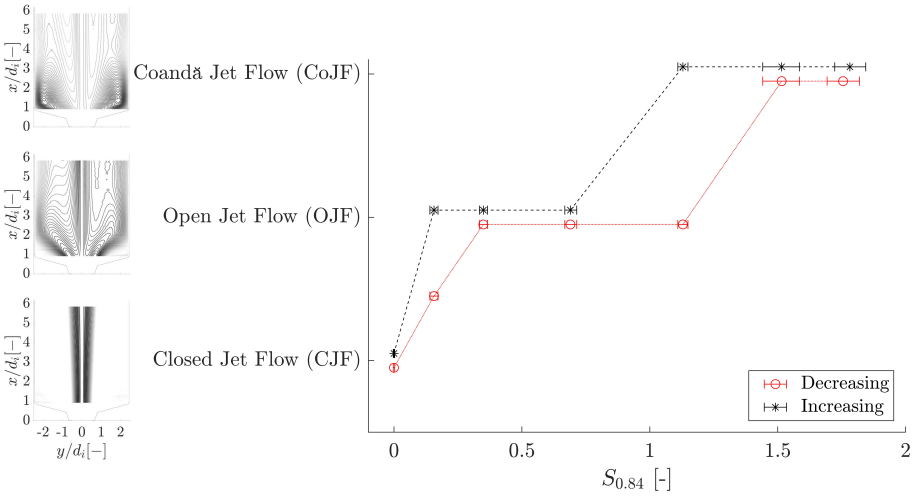

FIG. 11: Flow patterns identified of a swirling jet downstream of a two-step conical expansion and its transition map related to changing swirl number. A representative stream function plot of each flow pattern is added to the figure.

files, and stream functions. As the swirl increases, the occurrence of VB marks the transition towards an OJF. This VB bubble originates upstream of the inlet tube, as in the LDV measurements in Figure 5, it is not yet visible. The bubble behaves like a bluff body to the flow in the inlet tube, creating a central jet in the middle of the geometry. As the swirl number increases, the size of this bubble grows and it moves more upstream in the inlet tube, hence blocking the flow more. Due to the conservation of angular momentum, $r\omega$, the central jets rotates faster and faster in the wake of the bubble. This fast rotation induces radial pressure gradients, i.e.

$$\frac{\partial p}{\partial r} = \rho \frac{V_z^2}{r}. \tag{7}$$

If the radial expansion of the flow is sufficiently large, the Coanda effect in the sudden expansion pulls the jet towards the wall, similar to annular jet flows with a stepped-conical expansion[25]. If the swirl number is decreased from maximum swirl, the opposite effect occurs. The VB bubble size decreases and hysteretic behavior of VB[14] is most likely responsible for the hysteresis at $S_{0.84}$ = 1.13. Further decreasing the swirl reduces the size of the bubble and moves its location upstream of the inlet tube. This results in a decrease in radial expansion of the OJF. For $S_{0.84} = 0.35\downarrow$, a profile with a subtle OJF is observed, pushing the VB almost fully into the nozzle. In some cases in the literature, i.e., Moise and Mathew [14], CoJF flow can be reached if the swirl number is increased enough and will only disappear at a lower swirl number. In previous one-step conical expansion research, CoJF was reached only by decreasing the swirl number and not in the increasing case[26,29]. The hysteresis shown in Figure 11 is inverse to these expectations. This implies that low swirl numbers cannot be used to achieve CoJF in an SFR for enhancing efficiency. OJF appears more stable than CoJF at high swirl numbers for a two-step conical expansion, as is noted in Figure 11.

In the decreasing swirl case, a similar precessing structure, as discussed in Section III A is present in the flow field with a Strouhal number of 0.0028, at zero swirl. The jet spreading can be quantified using the jet half-width or the opening angle. The jet half-width is defined as the angle of the line connecting locations where the axial velocity is 50% of the jet's centerline velocity. The opening angle is defined as the line connecting locations where the axial velocity crosses zero. The decreasing swirl case with $S = 0$ shows slightly higher values for jet spreading compared to the starting case. Specifically, there is an increase of 2.27° and 3.26°, for the jet-half width and opening angle, respectively. However, both variables exhibit a high spread for this type of flow, as shown in Holemans *et al.* [34], with a standard deviation of 0.40 and 0.59, respectively.

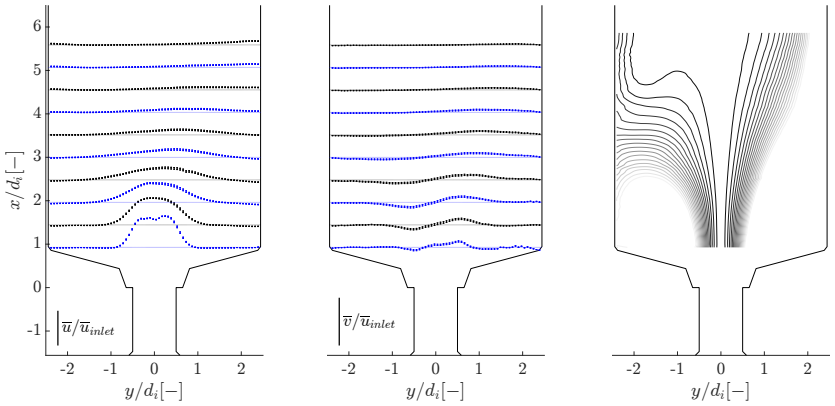

FIG. 12: Visualization of a non-axisymmetric jet at $S_{0.84} = 0.16\downarrow$, displayed in the geometry. Identical figure composition as Figure 8. (a) Axial velocity profiles. (b) Radial velocity profiles. (c) Stream function (ϕ).

The dimensionless maximum of the tangential velocity, in the S-PIV measurements, is three times higher for the decreasing swirl case than an equivalent increasing case. Similar behavior is noted in the LDV measurements, where a residual tangential velocity in the nozzle is observed. While decreasing the swirl number, at a low swirl number ($S_{0.84} = 0.16$), a non-axisymmetric jet is observed, visualized in Figure 12. The time-averaged flow field of the jet shows a deviation of the jet for the axial and radial velocity to one side, with its right side opening up and its left side exhibiting some recirculation. From $S_{0.84} = 1.52\uparrow$ and only until $S_{0.84} = 1.76\downarrow$, a double peak axial velocity forms at a sufficient distance from the expansion. Some hysteresis effects are also observed in the LDV measurements, where the tangential velocity remained higher at low swirl numbers $S_{0.84} < 0.25$ for the decreasing swirl case. At higher swirl numbers, no hysteresis behavior is observed in the nozzle neither for the velocity magnitudes, nor for the temporal spectra.

V. DYNAMICS OF FLOW PATTERNS

It is well known that swirling flows are inherently unsteady and can feature complex structures like VB or PVCs. To unravel the large scale coherent structures, a POD analysis was performed on the OJF and the CoJF. Results show that the coherent structures of both the OJF and CoJF are very

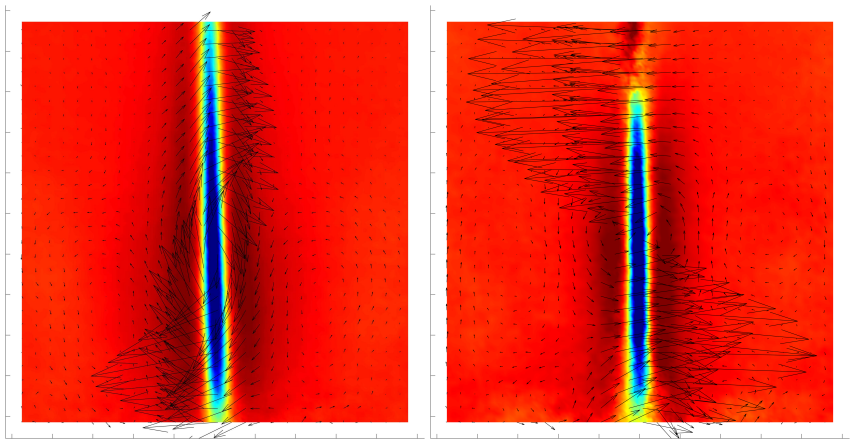

(a) (b)

FIG. 13: Spatial POD modes with the highest energy content for the CoJF at $S_{0.84}$ = 1.13. The vectors denote the in-plane velocity vectors, while the out-of-plane velocity is depicted by the color values. The colorbar is in arbitrary units to increase visibility. (a) Mode one of the pair. (b) Mode two of the pair.

similar at all swirl numbers and hence only 2 representative flow fields are shown, corresponding to the hysteresis location at $S_{0.84}$=1.13 in Figure 11.

The mode pair with the highest energy content for the CoJF is shown in Figure 13. This pair describes a precession of the central jet behind the VB bubble and contains 25% of the total energy. This mode pair is identical to the one found in the work of Holemans et al.[35] at maximum swirl. The precession has a temporal dynamic of St = 0.04. The mode pair with the highest energy content for the OJF is shown in Figure 14. The spatial structure is very similar to the CoJF. This pair also describes a precession of the central jet behind the VB bubble and contains 20% of the total energy. The precession itself has a temporal dynamic of St = 0.03, slightly slower than the one of the CoJF. This difference is attributed to the large VB bubble at higher swirl numbers, creating a larger rotational velocity near the central axis for the CoJF compared to the OJF, as also discussed in the previous section.

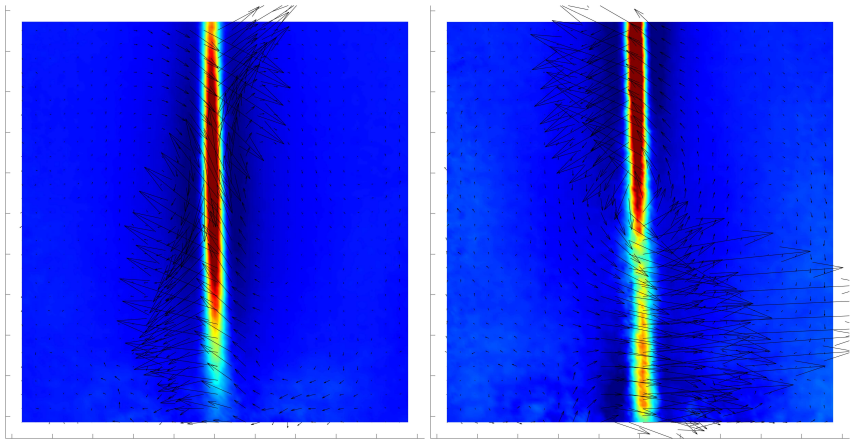

(a) (b)

FIG. 14: Spatial POD modes with the highest energy content for the OJF at $S_{0.84}$ = 1.13. The vectors denote the in-plane velocity vectors, while the out-of-plane velocity is depicted by the color values. The colorbar is in arbitrary units to increase visibility. (a) Mode one of the pair. (b) Mode two of the pair.

VI. CONCLUSIONS

A sudden expansion flow with a two-step conical expansion is characterized both upstream and downstream of the expansion by LDV and S-PIV measurements, respectively. A varying swirling flow inlet is calibrated by LDV measurements, which quantify the swirl number for 84% of the inlet tube's diameter, $S_{0.84}$. These values showed high axisymmetric similarity. The swirl number is increased and subsequently decreased to check for the hysteresis behavior of the flow field. Notably, the axial velocity profiles resembled power law velocity profiles at low swirl numbers. However, increasing swirl numbers led to a decreased central axial velocity until flow reversal, attributed to VB, occurred beyond $S_{0.84} = 1.74$. From $S_{0.84} \geq 0.48$ onwards, a PVC is observable in the frequency spectra, and up to the third harmonic is identified for the highest swirl numbers. At high swirl numbers, no hysteresis behavior of the jet is observed in the nozzle, neither for the velocity profiles nor the frequency spectra. A residual tangential velocity stays present at low swirl numbers while decreasing the swirl number, which promotes the precessing jet structure at these low swirl numbers and increases jet spreading. S-PIV measurements identify three different

flow structures: CJF, OJF, and CoJF. CJF is reached at zero swirl, which transitions to OJF for $0.16\uparrow \leq S_{0.84} \leq 0.69\uparrow$. CoJF is observed for $S_{0.84} \geq 1.13\uparrow$.

If VB is present, which is for OJF and CoJF, a positive central axial velocity emerges in combination with a radially expanding jet due to the contracting outlet. At decreasing swirl numbers, CoJF exists for $S_{0.84} \geq 1.52\downarrow$, and OJF exists for $0.35\downarrow \leq S_{0.84} \leq 1.13\downarrow$. The following pairs denote these pairs by first stating the increasing swirl number and then the decreasing swirl number: $S_{0.84} = [0.16; 0.69]$, $S_{0.84} = [0.13; 1.52]$ and $S_{0.84} = [0.35; 1.13]$, showing hysteretic behavior at $S_{0.84} = 1.13$. This hysteretic behavior is most likely caused by hysteresis in the appearance of VB as a function of the swirl number. Follow up research could address this by performing numerical simulations to reveal the flow structures in the nozzle and study the influence of Reynolds number on the characteristics of VB. With the findings in this study, flow control applications where the swirl number is the controlling parameter could be designed to switch between flow patterns in mixing applications, or switch flame patterns in swirl burners.

FUNDING

This work was supported by 'Dienst onderzoekscoördinatie (DOC) KU Leuven' [grant number C3/19/015].

DATA AVAILABILITY STATEMENT

Additional data that support the findings in this study are available from the corresponding author upon reasonable request.

CONFLICT OF INTEREST STATEMENT

The authors have no conflicts to disclose.

Appendix A: Refraction calculation for measuring velocities by LDV in the inlet tube

The ray-tracing of the LDV laser is explained in this Appendix. The formulas and nomenclature are based on Figure 4. The values for x_1, x_2, x_3, and y_1 are known in advance since they are specific to the setup, and can be derived from the values given in Section II B. All other values can

be calculated by ray tracing them. Using trigonometry, y_2 can be calculated,

$$y_2 = y_1 - tan(\alpha_1)\,(x_2 - x_1). \tag{A1}$$

The view box is made from PMMA with a different refractive index (n_{PMMA}) as the surrounding air (n_{air}). Based on Snell's law, this results in a refracted angle, α_2.

$$\alpha_2 = arcsin\left(\frac{n_{air}}{n_{PMMA}}\,sin(\alpha_1)\right). \tag{A2}$$

The entry point into the liquid, y_3, is calculated with trigonometry, which is

$$y_3 = y_2 - tan(\alpha_2)\,p_1. \tag{A3}$$

Using Snell's law again, α_3 can be calculated,

$$\alpha_3 = arcsin\left(\frac{n_{PMMA}}{n_{water}}\,sin(\alpha_2)\right). \tag{A4}$$

The ray of light will intersect with the outer circle of the inlet tube. This intersection point [x_4,y_4] is calculated by combining trigonometry and the equation for a circle into one system of equations. This system of equations will give two distinct solutions. The only correct solution is where $x_4 < 0$,

$$\begin{cases} y_3 - y_4 = tan(\alpha_3)\,(x_4 - x_3) \\ x_4^2 + y_4^2 = (R + p_2)^2. \end{cases} \tag{A5}$$

An extra line is introduced, which connects the point $[x_4, y_4]$ and the origin. The angle between this line and the horizontal line is α_8. This can be calculated using trigonometry,

$$\alpha_8 = -arctan\left(\frac{y_4}{x_4}\right). \tag{A6}$$

Two cases are identified: the measurement takes place in front ($\alpha_8 < \alpha_3$) or behind ($\alpha_8 > \alpha_3$) the tube's center. In the following equations, a $\pm$ or $\mp$ is used to distinguish between these two cases. For $\alpha_8 > \alpha_3$, the top sign is valid and for $\alpha_8 < \alpha_3$, the bottom sign is valid. No refractions occur at the moment that $\alpha_8 = \alpha_3$, and the ray trace will not change direction. This equality only happens if the measurement volume is at the exact center of the tube. The incident angle on the outer circle, α_4, can be calculated with Equation A7,

$$\alpha_4 = |\alpha_8 - \alpha_3|. \tag{A7}$$

The refractive angle inside the outer circle, α_5, follows from Snell's law,

$$\alpha_5 = arcsin\left(\frac{n_{water}}{n_{PMMA}} sin(\alpha_4)\right). \tag{A8}$$

For the intersection point on the inner circle of the inlet tube, x_5 and y_5, a combination of trigonometry and the equation for a circle is used in a system of equations. Two distinct solutions will follow from this system, for which only the one where $x_5 < 0$ is valid, as explained above.

$$\begin{cases} y_4 - y_5 = -tan(\alpha_8 \mp \alpha_5)(x_5 - x_4) \\ x_5^2 + y_5^2 = R^2 \end{cases} \tag{A9}$$

A second extra line connects the point $[x_5, y_5]$ and the origin. The angle between this line and the horizontal line is α_9. This angle is calculated by using trigonometry,

$$\alpha_9 = -arctan(\frac{y_5}{x_5}). \tag{A10}$$

The angle α_6 is the angle between the second extra line, the ray trace, and the incident angle on the inner circle,

$$\alpha_6 = \alpha_5 \pm \alpha_9 \mp \alpha_8. \tag{A11}$$

The refractive angle inside the inner circle, α_7, follows from Snell's law

$$\alpha_7 = arcsin\left(\frac{n_{PMMA}}{n_{water}} sin(\alpha_6)\right). \tag{A12}$$

The intersection position of the ray trace and the horizontal line, x_6, can be found using trigonometry and considering the angles α_8 and α_3. The two lasers of the LDV probe intersect at this point, where the measurement volume is also located. The reflected laser signal follows the same path described in the equations above,

$$x_6 = \frac{y_5}{tan(\alpha_9 \mp \alpha_7)} + x_5. \tag{A13}$$

Using trigonometry, α_{10} is obtained. This value is needed to calculate the fringe spacing created due to the intersecting laser beams,

$$\alpha_{10} = arctan\left(\frac{y_5}{x_6 - x_5}\right). \tag{A14}$$

Equation A15 calculates the fringe spacing. In a non-refracting case, α_{10} would be equal to α_1. In the axial measurements, the fringe spacing remains unchanged since the change in refractive index and the incident angle cancel each other out. In the tangential measurement, the fringe spacing

does change due to the refractions, for which Equation A15 describes this change. The LDV velocity output values must be scaled with the ratio between $d_{f,tangential}$ and the original fringe spacing, both values noted in Table II,

$$d_{f,tangential} = \frac{\lambda_{water}}{2\,sin(\alpha_{10})}. \tag{A15}$$

Equations A14 and A15 recalculate the fringe spacing based on the refractions, with λ_{water} being the wavelength of the LDV laser in the water medium, which is the original wavelength divided by the refractive index of the medium. These formulas are inspired by a study of Gardavsky *et al.*[57]. The equations are reformatted to have similar equations for each interface, which makes the calculations less complex.

II. VELOCITY PROFILES OF WHOLE HYSTERESIS

A. Axial velocity profiles

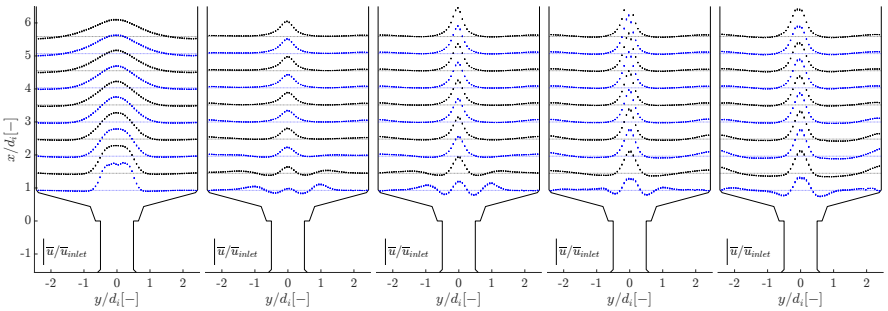

(a) $S_{0.84} = 0$ (b) $S_{0.84} = 0.16\uparrow$ (c) $S_{0.84} = 0.35\uparrow$ (d) $S_{0.84} = 0.69\uparrow$ (e) $S_{0.84} = 1.13\uparrow$

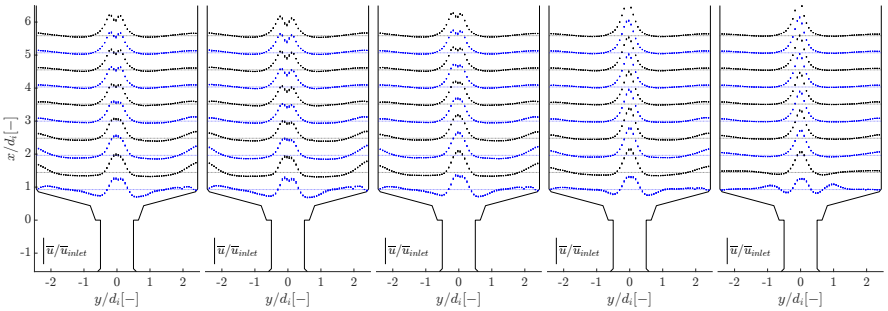

(f) $S_{0.84} = 1.52\uparrow$ (g) $S_{0.84} = 1.78\uparrow$ (h) $S_{0.84} = 1.76\downarrow$ (i) $S_{0.84} = 1.52\downarrow$ (j) $S_{0.84} = 1.13\downarrow$

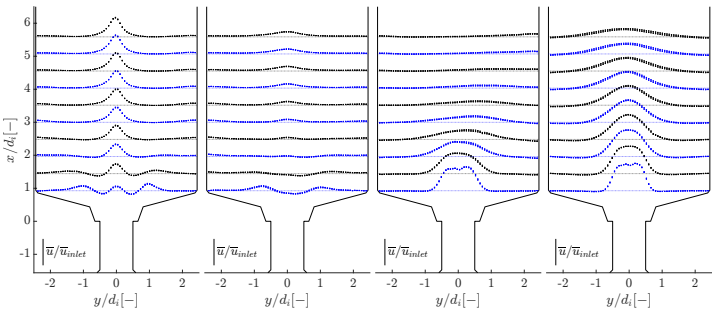

(k) $S_{0.84} = 0.69\downarrow$ (l) $S_{0.84} = 0.35\downarrow$ (m) $S_{0.84} = 0.16\downarrow$ (n) $S_{0.84} = 0\downarrow$

FIG. 15: Axial velocity profiles plotted in the geometry for all S-PIV measurements, both increasing (↑) and decreasing (↓) swirl. Identical figure composition as Figure 15.

B. Radial velocity profiles

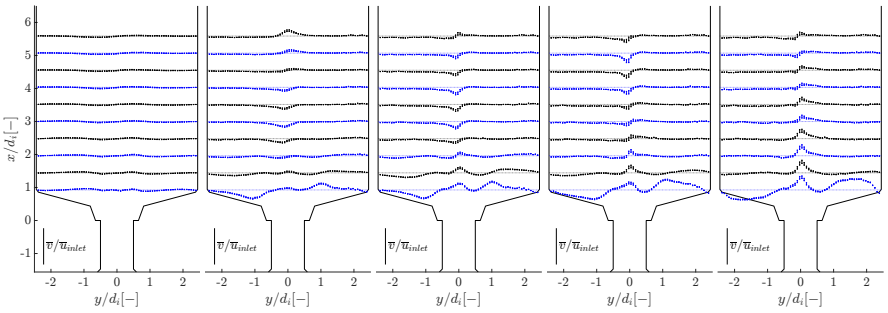

(a) $S_{0.84} = 0$ (b) $S_{0.84} = 0.16\uparrow$ (c) $S_{0.84} = 0.35\uparrow$ (d) $S_{0.84} = 0.69\uparrow$ (e) $S_{0.84} = 1.13\uparrow$

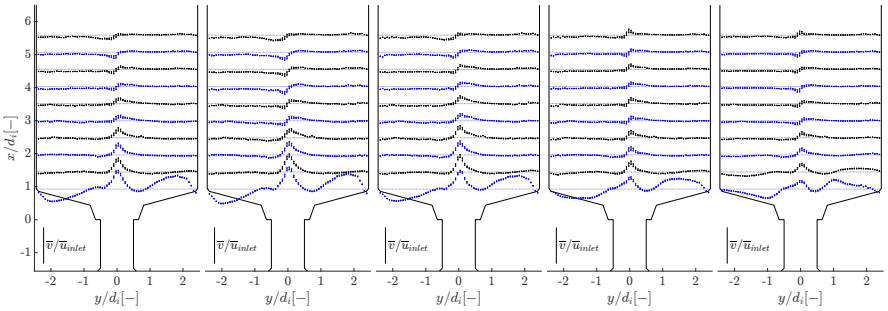

(f) $S_{0.84} = 1.52\uparrow$ (g) $S_{0.84} = 1.78\uparrow$ (h) $S_{0.84} = 1.76\downarrow$ (i) $S_{0.84} = 1.52\downarrow$ (j) $S_{0.84} = 1.13\downarrow$

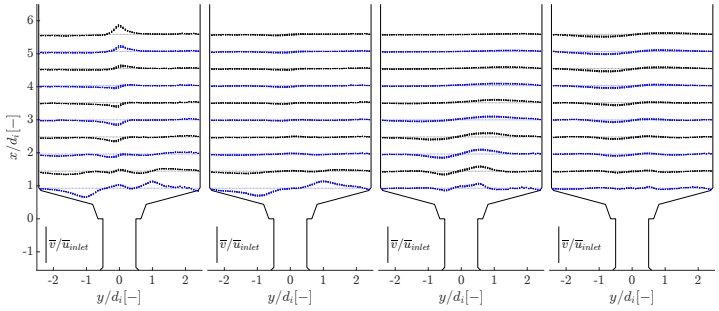

(k) $S_{0.84} = 0.69\downarrow$ (l) $S_{0.84} = 0.35\downarrow$ (m) $S_{0.84} = 0.16\downarrow$ (n) $S_{0.84} = 0\downarrow$

FIG. 16: Radial velocity profiles plotted in the geometry for all S-PIV measurements, both increasing (↑) and decreasing (↓) swirl. Identical figure composition as Figure 15.

C. Tangential velocity profiles

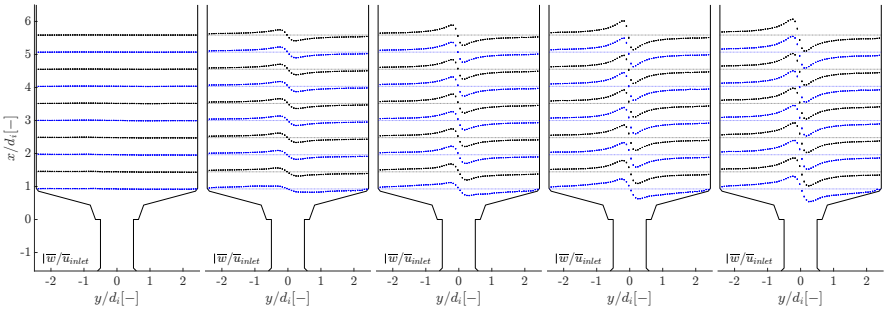

(a) $S_{0.84} = 0$ (b) $S_{0.84} = 0.16\uparrow$ (c) $S_{0.84} = 0.35\uparrow$ (d) $S_{0.84} = 0.69\uparrow$ (e) $S_{0.84} = 1.13\uparrow$

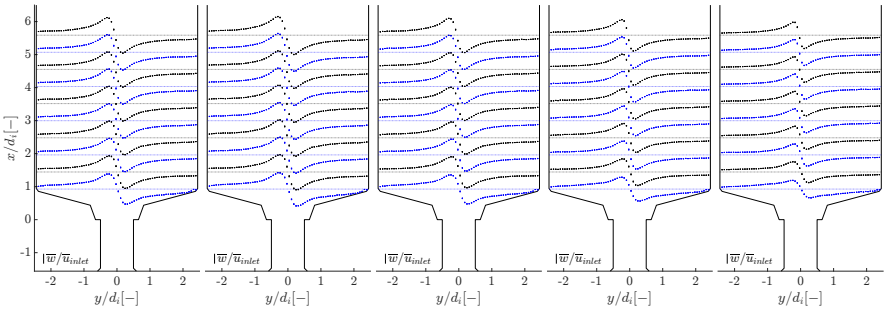

(f) $S_{0.84} = 1.52\uparrow$ (g) $S_{0.84} = 1.78\uparrow$ (h) $S_{0.84} = 1.76\downarrow$ (i) $S_{0.84} = 1.52\downarrow$ (j) $S_{0.84} = 1.13\downarrow$

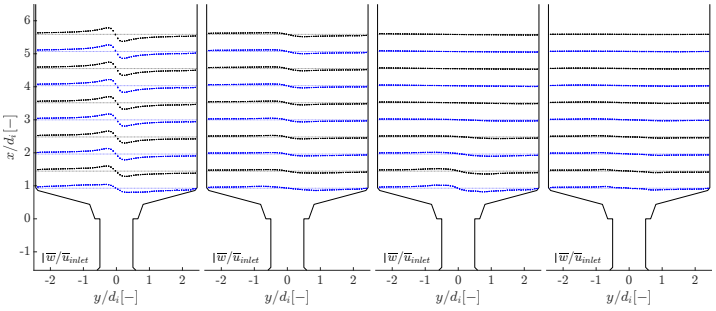

(k) $S_{0.84} = 0.69\downarrow$ (l) $S_{0.84} = 0.35\downarrow$ (m) $S_{0.84} = 0.16\downarrow$ (n) $S_{0.84} = 0\downarrow$

FIG. 17: Tangential velocity profiles plotted in the geometry for all S-PIV measurements, both increasing (↑) and decreasing (↓) swirl. Identical figure composition as Figure 15.

III. RMS PROFILES OF ALL DATA SETS

A. Axial RMS profiles

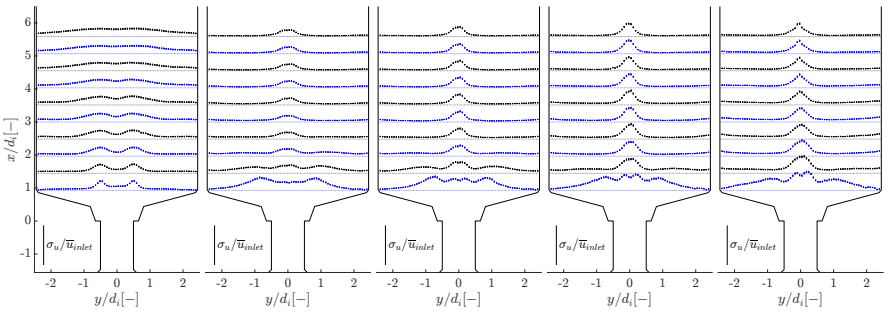

(a) $S_{0.84} = 0$ (b) $S_{0.84} = 0.16\uparrow$ (c) $S_{0.84} = 0.35\uparrow$ (d) $S_{0.84} = 0.69\uparrow$ (e) $S_{0.84} = 1.13\uparrow$

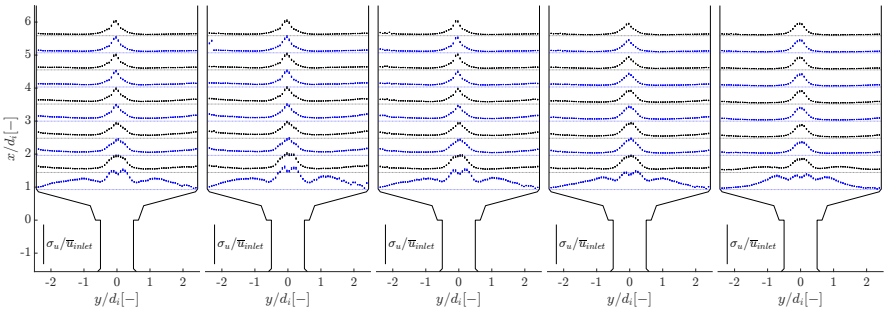

(f) $S_{0.84} = 1.52\uparrow$ (g) $S_{0.84} = 1.78\uparrow$ (h) $S_{0.84} = 1.76\downarrow$ (i) $S_{0.84} = 1.52\downarrow$ (j) $S_{0.84} = 1.13\downarrow$

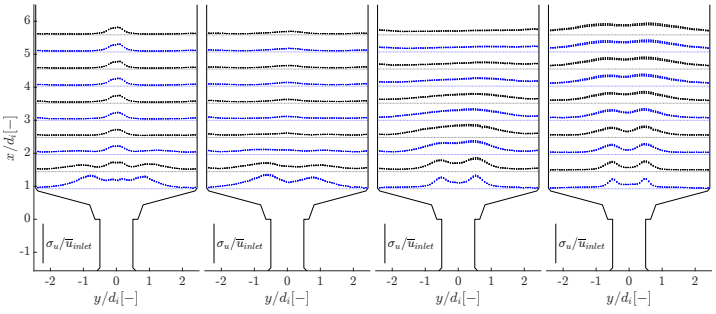

(k) $S_{0.84} = 0.69\downarrow$ (l) $S_{0.84} = 0.35\downarrow$ (m) $S_{0.84} = 0.16\downarrow$ (n) $S_{0.84} = 0\downarrow$

FIG. 18: Axial RMS velocity profiles plotted in the geometry for all S-PIV measurements, both increasing (↑) and decreasing (↓) swirl. Identical figure composition as Figure 15.

B. Radial RMS profiles

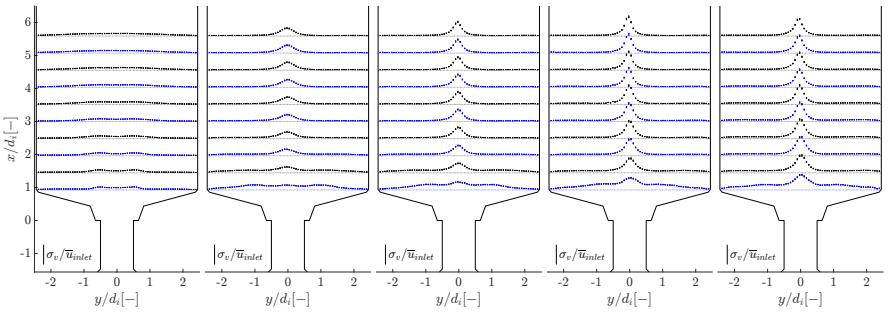

(a) $S_{0.84} = 0$ (b) $S_{0.84} = 0.16\uparrow$ (c) $S_{0.84} = 0.35\uparrow$ (d) $S_{0.84} = 0.69\uparrow$ (e) $S_{0.84} = 1.13\uparrow$

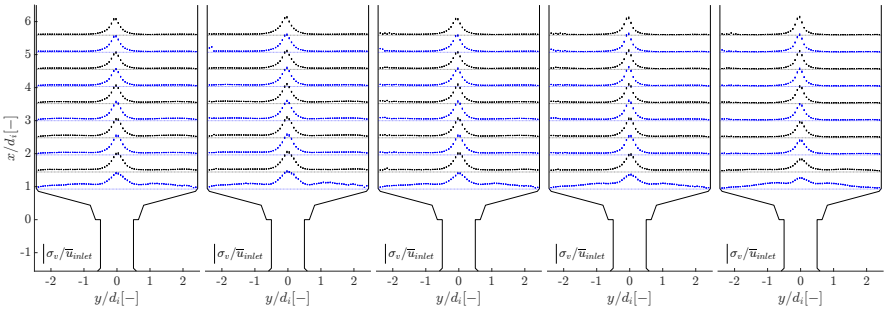

(f) $S_{0.84} = 1.52\uparrow$ (g) $S_{0.84} = 1.78\uparrow$ (h) $S_{0.84} = 1.76\downarrow$ (i) $S_{0.84} = 1.52\downarrow$ (j) $S_{0.84} = 1.13\downarrow$

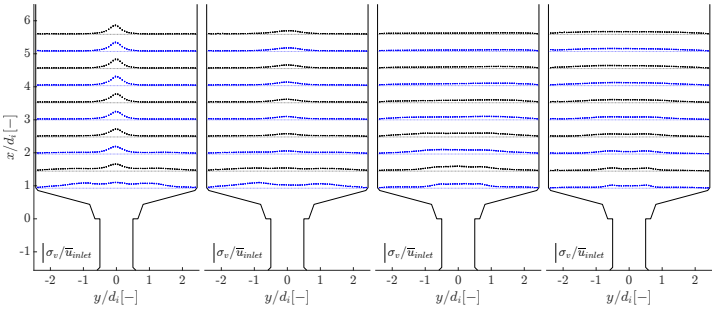

(k) $S_{0.84} = 0.69\downarrow$ (l) $S_{0.84} = 0.35\downarrow$ (m) $S_{0.84} = 0.16\downarrow$ (n) $S_{0.84} = 0\downarrow$

FIG. 19: Radial RMS velocity profiles plotted in the geometry for all S-PIV measurements, both increasing (↑) and decreasing (↓) swirl. Identical figure composition as Figure 15.

C. Tangential RMS profiles

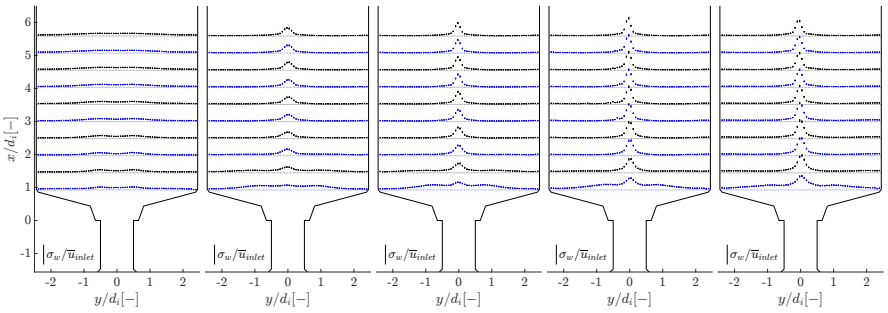

(a) $S_{0.84} = 0$ (b) $S_{0.84} = 0.16\uparrow$ (c) $S_{0.84} = 0.35\uparrow$ (d) $S_{0.84} = 0.69\uparrow$ (e) $S_{0.84} = 1.13\uparrow$

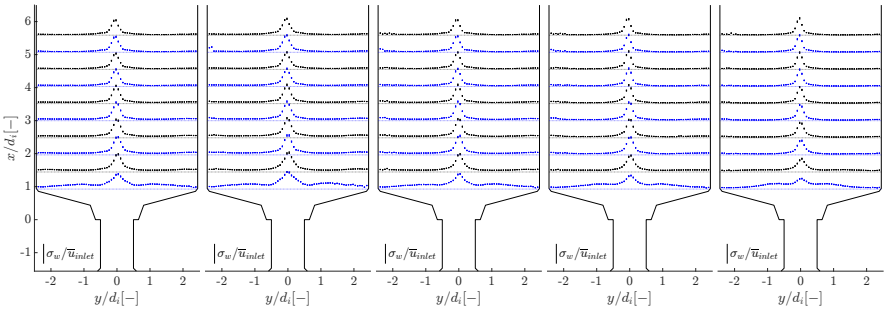

(f) $S_{0.84} = 1.52\uparrow$ (g) $S_{0.84} = 1.78\uparrow$ (h) $S_{0.84} = 1.76\downarrow$ (i) $S_{0.84} = 1.52\downarrow$ (j) $S_{0.84} = 1.13\downarrow$

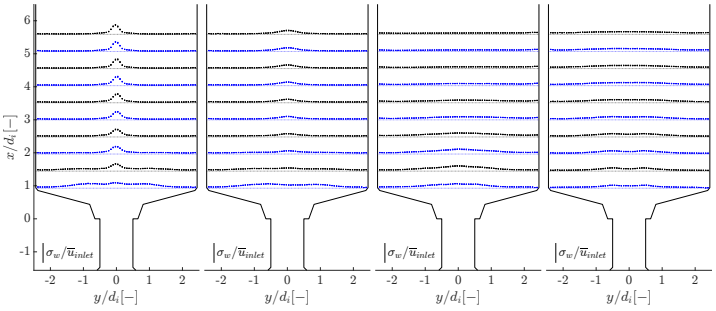

(k) $S_{0.84} = 0.69\downarrow$ (l) $S_{0.84} = 0.35\downarrow$ (m) $S_{0.84} = 0.16\downarrow$ (n) $S_{0.84} = 0\downarrow$

FIG. 20: Tangential RMS velocity profiles plotted in the geometry for all S-PIV measurements, both increasing (↑) and decreasing (↓) swirl. Identical figure composition as Figure 15.

IV. STREAM FUNCTIONS (ϕ) OF ALL DATA SETS

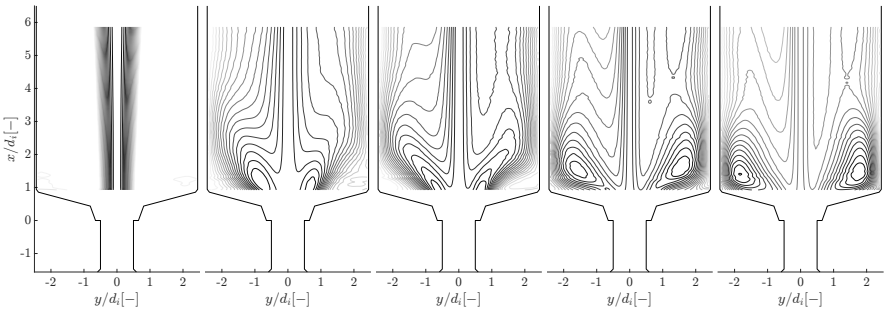

(a) $S_{0.84} = 0$ (b) $S_{0.84} = 0.16\uparrow$ (c) $S_{0.84} = 0.35\uparrow$ (d) $S_{0.84} = 0.69\uparrow$ (e) $S_{0.84} = 1.13\uparrow$

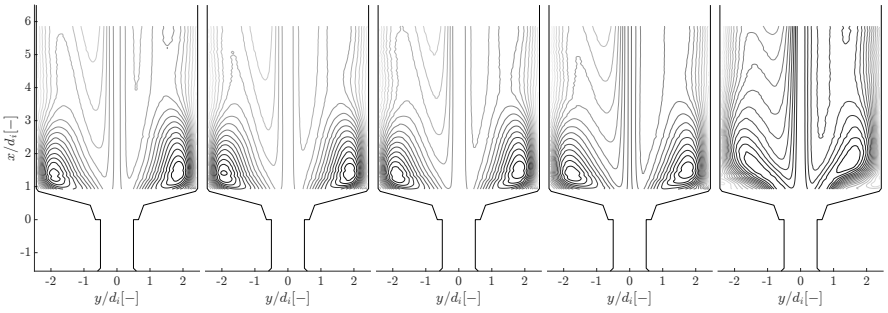

(f) $S_{0.84} = 1.52\uparrow$ (g) $S_{0.84} = 1.78\uparrow$ (h) $S_{0.84} = 1.76\downarrow$ (i) $S_{0.84} = 1.52\downarrow$ (j) $S_{0.84} = 1.13\downarrow$

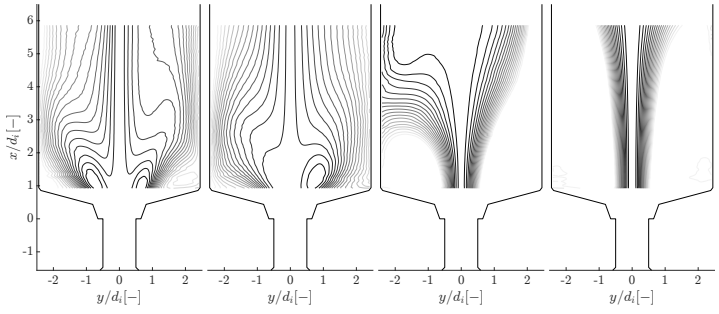

(k) $S_{0.84} = 0.69\downarrow$ (l) $S_{0.84} = 0.35\downarrow$ (m) $S_{0.84} = 0.16\downarrow$ (n) $S_{0.84} = 0\downarrow$

FIG. 21: Stream function ϕ plotted in the geometry for all S-PIV measurements, both increasing ($\uparrow$) and decreasing ($\downarrow$) swirl.

V. IN-PLANE VECTOR PLOTS OF ALL DATA SETS

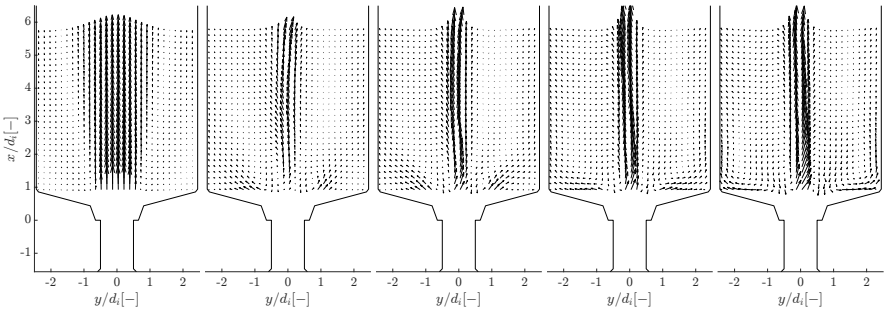

(a) $S_{0.84} = 0$ (b) $S_{0.84} = 0.16\uparrow$ (c) $S_{0.84} = 0.35\uparrow$ (d) $S_{0.84} = 0.69\uparrow$ (e) $S_{0.84} = 1.13\uparrow$

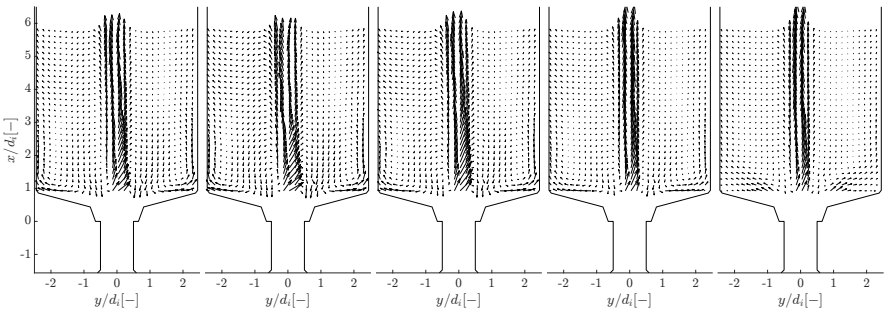

(f) $S_{0.84} = 1.52\uparrow$ (g) $S_{0.84} = 1.78\uparrow$ (h) $S_{0.84} = 1.76\downarrow$ (i) $S_{0.84} = 1.52\downarrow$ (j) $S_{0.84} = 1.13\downarrow$

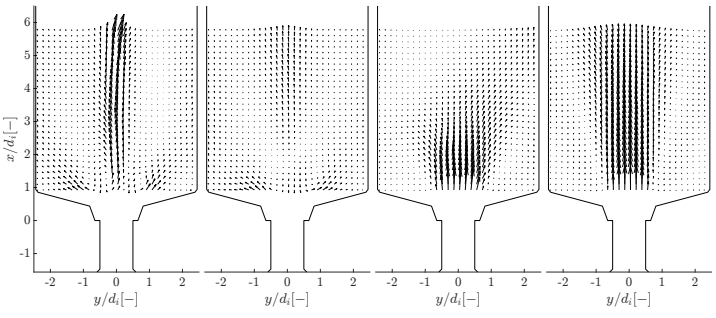

(k) $S_{0.84} = 0.69\downarrow$ (l) $S_{0.84} = 0.35\downarrow$ (m) $S_{0.84} = 0.16\downarrow$ (n) $S_{0.84} = 0\downarrow$

FIG. 22: In-plane vectors plotted in the geometry for all S-PIV measurements, both increasing (↑) and decreasing (↓) swirl.

REFERENCES

[1]A. Gupta, D. Lilley, and N. Syred, *Swirl Flows*, Energy and Engineering Science Series (Abacus Press, 1984).

[2]S. Burmberger and T. Sattelmayer, "Optimization of the Aerodynamic Flame Stabilization for Fuel Flexible Gas Turbine Premix Burners," Journal of Engineering for Gas Turbines and Power **133**, 101501 (2011).

[3]I. Chterev, G. Sundararajan, J. M. Seitzman, and T. C. Lieuwen, "Precession Effects on the Relationship Between Time-Averaged and Instantaneous Swirl Flow and Flame Characteristics," in *Volume 4A: Combustion, Fuels and Emissions* (American Society of Mechanical Engineers, Montreal, Quebec, Canada, 2015) p. V04AT04A061.

[4]S. H. Park and H. D. Shin, "Measurements of entrainment characteristics of swirling jets," International Journal of Heat and Mass Transfer **36**, 4009–4018 (1993).

[5]Z. Yang, T. Holemans, B. Lagrain, B. Sels, and M. Vanierschot, "A solid-liquid mixing reactor based on swirling flow technology," Chemical Engineering Science **280**, 119054 (2023).

[6]N. Syred, "A review of oscillation mechanisms and the role of the precessing vortex core (PVC) in swirl combustion systems," Prog Energy Combust Sci **32**, 93–161 (2006).

[7]T. Holemans, Z. Yang, J. De Greef, S. Van Den Bosch, and M. Vanierschot, "Experimental study of precessing instabilities in the cold flow field of a sudden expansion dump combustor," in *Proceedings of 20th International Symposium on Application of Laser and Imaging Techniques to Fluid Mechanics* (Lisbon, 2022) pp. 2752–2765.

[8]O. Lucca-Negro and T. O'Doherty, "Vortex breakdown: A review," Progress in Energy and Combustion Science **27**, 431–481 (2001).

[9]M. Vanierschot, "Large scale flow instabilities in sudden expansion flows in the subcritical swirl regime," in *Proceedings of 19th International Symposium on Application of Laser and Imaging Techniques to Fluid Mechanics* (Lisbon, Portugal, 2018) pp. 2215–2224.

[10]T. B. Benjamin, "Theory of the vortex breakdown phenomenon," Journal of Fluid Mechanics **14**, 593 (1962).

[11]S. Leibovich, "Vortex stability and breakdown - Survey and extension," AIAA Journal **22**, 1192–1206 (1984).

[12]M. G. Hall, "Vortex Breakdown," Annual Review of Fluid Mechanics **4**, 195–218 (1972).

[13]M. Sharma and A. Sameen, "On the correlation between vortex breakdown bubble and planar

helicity in Vogel–Escudier flow," Journal of Fluid Mechanics **888**, A6 (2020).

[14]P. Moise and J. Mathew, "Hysteresis and turbulent vortex breakdown in transitional swirling jets," Journal of Fluid Mechanics **915**, A94 (2021).

[15]P. Moise, "An assessment of theories modeling vortex breakdown as a transition between cylindrical flow states," Physics of Fluids **32**, 123601 (2020).

[16]C. M. Douglas and L. Lesshafft, "Confinement effects in laminar swirling jets," Journal of Fluid Mechanics **945**, A27 (2022).

[17]F. Selimefendigil and H. F. Öztop, "Effects of local curvature and magnetic field on forced convection in a layered partly porous channel with area expansion," International Journal of Mechanical Sciences **179**, 105696 (2020).

[18]A. Kimouche, A. Mataoui, H. F. Oztop, and N. Abu-Hamdeh, "Analysis of heat transfer of different nanofluids flow through an abrupt expansion pipe," Applied Thermal Engineering **112**, 965–974 (2017).

[19]H. Oztop and I. Dagtekin, "Enhancement of heat transfer in a pipe with inner contraction-expansion-contraction pipe insertion," International Communications in Heat and Mass Transfer **30**, 1157–1168 (2003).

[20]G. Li and E. J. Gutmark, "Effect of exhaust nozzle geometry on combustor flow field and combustion characteristics," Proceedings of the Combustion Institute **30**, 2893–2901 (2005).

[21]S. Terhaar, B. C. Bobusch, and C. O. Paschereit, "Effects of Outlet Boundary Conditions on the Reacting Flow Field in a Swirl-Stabilized Burner at Dry and Humid Conditions," Journal of Engineering for Gas Turbines and Power **134**, 111501 (2012).

[22]N. Syred and K. Dahman, "Effect of high levels of confinement upon the aerodynamics of swirl burners," Journal of Energy **2**, 8–15 (1978).

[23]M. P. Escudier, A. K. Nickson, and R. J. Poole, "Influence of outlet geometry on strongly swirling turbulent flow through a circular tube," Physics of Fluids **18**, 125103 (2006).

[24]A. Nejad and S. Ahmed, "Flow field characteristics of an axisymmetric sudden-expansion pipe flow with different initial swirl distribution," International Journal of Heat and Fluid Flow **13**, 314–321 (1992).

[25]M. Vanierschot, *Fluid Mechanics and Control of Annular Jets with and without Swirl*, Ph.D. thesis, KU Leuven, Leuven (2007).

[26]G. Ogus, M. Baelmans, and M. Vanierschot, "On the flow structures and hysteresis of laminar swirling jets," Physics of Fluids **28**, 123604 (2016).

[27]Y. Zhang and M. Vanierschot, "Determination of single and double helical structures in a swirling jet by spectral proper orthogonal decomposition," Physics of Fluids **33**, 015115 (2021).

[28]Z. Yang, V. Castaneda, G. Ogus, T. Holemans, M. Vanierschot, and A. Valera-Medina, "Identification and dynamics of coherent structures in a Coanda swirling jet flow," Experimental Thermal and Fluid Science **142**, 110817 (2023).

[29]M. Vanierschot and E. Van den Bulck, "Hysteresis in flow patterns in annular swirling jets," Experimental Thermal and Fluid Science **31**, 513–524 (2007).

[30]M. Vanierschot and E. Van den Bulck, "Influence of the nozzle geometry on the hysteresis of annular swirling jets," Combustion Science and Technology **179**, 1451–1466 (2007).

[31]Z. Yang, T. Holemans, B. Lagrain, B. Sels, and M. Vanierschot, "A draft tube to improve mixing in swirling flow-based solid–liquid mixing reactors," Chemical Engineering Research and Design **206**, 226–241 (2024).

[32]J. Dugué and R. Weber, "Design and calibration of a 30kw natural gas burner for the University of Michigan." Technical Report C74/y/1. (International Flame Research Foundation (IFRF), Ijmuiden, The Netherlands, 1992).

[33]M. Vanierschot, J. S. Müller, M. Sieber, M. Percin, B. W. van Oudheusden, and K. Oberleithner, "Single- and double-helix vortex breakdown as two dominant global modes in turbulent swirling jet flow," Journal of Fluid Mechanics **883**, A31 (2020).

[34]T. Holemans, Z. Yang, J. De Greef, and M. Vanierschot, "Experimental study of a self-excited jet precession in a sudden expansion flow," Experiments in fluids **64**, 107 (2023).

[35]T. Holemans, Z. Yang, J. De Greef, and M. Vanierschot, "Simultaneous Existence of a Coandã and Central Jet Flow measured by Stereoscopic Particle Image Velocimetry," in *Proceedings of the 15th International Symposium on Particle Image Velocimetry* (San Diego, USA, 2023-06-19/2023-06-21).

[36]A. K. M. F. Hussain and W. C. Reynolds, "The mechanics of an organized wave in turbulent shear flow," Journal of Fluid Mechanics **41**, 241–258 (1970).

[37]G. Xu and R. Antonia, "Effect of different initial conditions on a turbulent round free jet," Experiments in Fluids **33**, 677–683 (2002).

[38]C. Y. Wong, G. J. Nathan, and T. O'Doherty, "The effect of initial conditions on the exit flow from a fluidic precessing jet nozzle," Experiments in Fluids **36**, 70–81 (2004).

[39]M. Ahmadvand, A. F. Najafi, and S. Shahidinejad, "Investigation on the Effects of Various Swirl Generators on Heat Transfer and Fluid Flow in Decaying Swirling Flows," Proceedings of the

Institution of Mechanical Engineers, Part C: Journal of Mechanical Engineering Science **224**, 2181–2197 (2010).

[40]G. Vignat, D. Durox, and S. Candel, "The suitability of different swirl number definitions for describing swirl flows: Accurate, common and (over-) simplified formulations," Progress in Energy and Combustion Science **89**, 100969 (2022).

[41]M. N. Polyanskiy, "Refractiveindex.info database of optical constants," Scientific Data **11**, 94 (2024).

[42]M. Vanierschot, K. Van Dyck, P. Sas, and E. Van den Bulck, "Symmetry breaking and vortex precession in low-swirling annular jets," Physics of Fluids **26**, 105110 (2014).

[43]M. Vanierschot and G. Ogus, "Experimental investigation of the precessing vortex core in annular swirling jet flows in the transitional regime," Experimental Thermal and Fluid Science **106**, 148–158 (2019).

[44]A. Sciacchitano, "Uncertainty quantification in particle image velocimetry," Measurement Science & Technology **30**, 092001 (2019).

[45]M. Raffel, C. E. Willert, F. Scarano, C. J. Kähler, S. T. Wereley, and J. Kompenhans, *Particle Image Velocimetry: A Practical Guide* (Springer International Publishing, Cham, 2018).

[46]P. Buchhave, W. K. George, and J. L. Lumley, "The Measurement of Turbulence with the Laser-Doppler Anemometer," Annual Review of Fluid Mechanics **11**, 443–503 (1979).

[47]W. K. George, "Quantitative measurement with the burst-mode laser Doppler anemometer," Experimental Thermal and Fluid Science **1**, 29–40 (1988).

[48]A. Sciacchitano and B. Wieneke, "PIV uncertainty propagation," Measurement Science and Technology **27**, 084006 (2016).

[49]Y. A. Çengel, *Fundamentals of Thermal-Fluid Sciences*, sixth edition. ed. (McGraw Hill, LLC, New York, NY, 2022).

[50]J. Mi, G. Nathan, and C. Wong, "The influence of inlet flow condition on the frequency of self-excited jet precession," Journal of Fluids and Structures **22**, 129–133 (2006).

[51]J. Mi, G. J. Nathan, and D. S. Nobes, "Mixing Characteristics of Axisymmetric Free Jets From a Contoured Nozzle, an Orifice Plate and a Pipe," Journal of Fluids Engineering **123**, 878–883 (2001).

[52]H. Liang and T. Maxworthy, "An experimental investigation of swirling jets," Journal of Fluid Mechanics **525**, 115–159 (2005).

[53]K. Oberleithner, C. O. Paschereit, R. Seele, and I. Wygnanski, "Formation of Turbulent Vortex

Breakdown: Intermittency, Criticality, and Global Instability," AIAA Journal **50**, 1437–1452 (2012).

[54]P. Welch, "The use of fast Fourier transform for the estimation of power spectra: A method based on time averaging over short, modified periodograms," IEEE Transactions on Audio and Electroacoustics **15**, 70–73 (1967).

[55]G. K. Batchelor, *An Introduction to Fluid Dynamics*, Cambridge Mathematical Library (Cambridge university press, Cambridge New York, 1967).

[56]M. Sieber, C. O. Paschereit, and K. Oberleithner, "Spectral proper orthogonal decomposition," Journal of Fluid Mechanics **792**, 798–828 (2016).

[57]J. Gardavsky, J. Hrbek, Z. Chara, and M. Severa, "Refraction corrections for LDA measurements in Circular Tubes within Rectangular Optical Boxes," Dantec Information **8**, 2–5 (1989).